



# Reconciling Surface Deflections From Simulations of Global Mantle Convection

Conor P. B. O'Malley<sup>1,a</sup>, Gareth G. Roberts<sup>1</sup>, James Panton<sup>2</sup>, Fred D. Richards<sup>1</sup>, J. Huw Davies<sup>2</sup>, Victoria M. Fernandes<sup>1,b</sup>, and Sia Ghelichkhan<sup>3</sup>

<sup>1</sup>Department of Earth Science & Engineering, Imperial College London, London SW7 2BP, UK

<sup>a</sup>now at Cathie Group, 2-4 Hanover Square, Newcastle upon Tyne, NE1 3NP, UK

<sup>2</sup>School of Earth & Environmental Sciences, University of Cardiff, Park Place, Cardiff CF10 3AT, UK

<sup>b</sup>now at Section 4.6 Geomorphology, GFZ Potsdam, Telegrafenberg, 14473 Potsdam, Germany

<sup>3</sup>Research School of Earth Sciences, Australian National University, 142 Mills Road, Acton, ACT 0200, Australia

**Correspondence:** Gareth G. Roberts (gareth.roberts@imperial.ac.uk)

**Abstract.** The modern state of the mantle and its evolution on geological timescales is of widespread importance for the Earth sciences. For instance, it is generally agreed that mantle flow is manifest in topographic and drainage network evolution, glacio-eustasy and in the distribution of sediments. There now exists a variety of theoretical approaches to predict histories of mantle convection and its impact on surface deflections. A general goal is to make use of observed deflections to identify Earth-like simulations and constrain the history of mantle convection. Several important insights into the role of radial and non-radial viscosity variations, gravitation, and the importance of shallow structure already exist. Here we seek to bring those insights into a single framework to elucidate the relative importance of popular modelling choices on predicted instantaneous vertical surface deflections. We start by comparing results from numeric and analytic approaches to solving the equations of motion that are ostensibly parameterised to be as-similar-as-possible. Resultant deflections can vary by  $\sim 10\%$ , increasing to  $\sim 25\%$  when viscosity is temperature-dependent. Including self-gravitation and gravitational potential of the deflected surface are relatively small sources of discrepancy. However, spherical harmonic correlations between model predictions decrease dramatically with the excision of shallow structure to increasing depths, and when radial viscosity structure is modified. The results emphasise sensitivity of instantaneous surface deflections to density and viscosity anomalies in the upper mantle. They reinforce the view that a detailed understanding of lithospheric structure is crucial for relating mantle convective history to observations of vertical motions at Earth's surface.

## 1 Introduction

Mantle convection plays a crucial role in Earth's evolution (e.g., Hager and Clayton, 1989; Parsons and Daly, 1983; Pekeris, 1935). It is well understood, for instance, that flow in the mantle is fundamental in the transfer of heat and chemicals from the deep Earth to the surface, in driving horizontal and vertical lithospheric motions (thus tectonic processes), and in magnetism via interactions with the core (e.g., Biggin et al., 2012; Davies et al., 2023; Foley and Fischer, 2017; Hoggard et al., 2016; Holdt et al., 2022; Pekeris, 1935). In turn, many processes operating at or close to Earth's surface are impacted, including glacio-



eustasy, magmatism, climate, sediment routing, natural resource distribution, drainage network evolution, and development of biodiversity (e.g., Bahadori et al., 2022; Ball et al., 2021; Braun, 2010; Chang and Liu, 2021; Hazzard et al., 2022; O'Malley et al., 2021; Salles et al., 2017; Stanley et al., 2021). Clearly, understanding the physical and chemical evolution of the mantle  
25 has broad implications. An important goal is to determine contributions to surface processes from the modern mantle and its history during, say, the last 100 million years.

Residual oceanic age-depth measurements, potential field data, seismic tomographic models and melting histories of young mafic rocks are providing increasingly coherent observational insights into the modern and recent state of the mantle (e.g., Ball  
30 et al., 2022; Davies et al., 2023; Fichtner et al., 2009, 2013; Fichtner and Villaseñor, 2015; French and Romanowicz, 2015; Hoggard et al., 2016; Holdt et al., 2022; Kaula, 1963; Lekić and Fischer, 2014; Priestley and McKenzie, 2013; Richards et al., 2023). Stratigraphic and geomorphic observations as well as magmatic histories provide clues about the history of mantle convection on geologic timescales (e.g., Al-Hajri et al., 2009; Czarnota et al., 2013; Flament et al., 2015; Fernandes et al., 2019; Fernandes and Roberts, 2021; Galloway et al., 2011; Gunnell and Burke, 2008; Gurnis et al., 2000; Hoggard et al., 2021;  
35 Lambeck et al., 1998; Morris et al., 2020; O'Malley et al., 2021; Stanley et al., 2021). Despite these advances, observations providing information about the history of mantle convection are sparse in places, especially within continental interiors and back in time (see e.g., Hoggard et al., 2021). Moreover, disentangling contributions from crustal, lithospheric and sub-lithospheric processes to surface deflections remains challenging and controversial (see e.g., Hoggard et al., 2021; Wang et al., 2022).

Theoretical approaches that retrodict histories of mantle convection can, in principle, be used to fill in spatio-temporal gaps in the observational record and disentangle contributions to surface observables from different geologic processes (e.g., Baumgardner, 1985; Bunge and Baumgardner, 1995; Davies et al., 2013; Flament et al., 2015; Ghelichkhan et al., 2021; Hager et al., 1985; Moucha and Forte, 2011; Steinberger and Antretter, 2006). Increasingly realistic geodynamic simulations incorporating, for instance, plate motions, gravitation and deflection of gravitational potential fields, complex rheologies, viscosity laws that  
45 can include temperature, pressure, composition, grain size and strain rate dependence, and assimilation of seismic tomographic information into flow solutions, result in a diverse array of retrodicted flow histories. Mineralogical phase changes, compressibility, different surface and core-mantle boundary slip conditions (e.g., no-slip, free-slip), chemical and thermal buoyancy, and plate motion constraints on mantle structure can also generate diverse predictions of mantle convection and resultant surface deflections (e.g., Baumgardner, 1985; Bunge et al., 2002, 2003; Corrieu et al., 1995; Cramer et al., 2012; Dannberg et al.,  
50 2017; Flament et al., 2014; Forte, 2007; Ghosh and Holt, 2012; Glišović and Forte, 2016; Hager and Clayton, 1989; Heister et al., 2017; Liu and Gurnis, 2008; Panasyuk et al., 1996; Ribe, 2007; Ricard, 2007; Tackley et al., 1993; Zhong et al., 2008; Zhou et al., 2018; Liu and King, 2019). Aside from the fundamental choice of governing equations and parameterizations underpinning simulations, mathematical and computational approaches to solve the equations of motion generate different predictions of surface deflections. These approaches sit within two broad families: numeric simulations (e.g., ASPECT, CitcomS, TERRA; Bangerth et al., 2023; Baumgardner, 1985; Zhong et al., 2000), and propagator-matrix-based, quasi-analytic  
55 techniques, that can be solved in two or three dimensions, and importantly for our purposes, spherically and spectrally (e.g.,



Colli et al., 2016; Hager and O’Connell, 1979; Parsons and Daly, 1983).

A challenge then is to establish whether observed surface deflections can be used to discriminate between theoretical predic-  
60 tions of mantle convection, and, in turn, identify models that generate realistic and testable retrodictions. In this study we are  
principally concerned with establishing similarities and sensitivities of predicted instantaneous vertical surface deflections. We  
focus on vertical motions for two reasons. First, inventories of measurements of uplift and subsidence—on timescales of mantle  
convection—now exist for most continents and could be compared to predictions from global simulations in future work (e.g.,  
Fernandes and Roberts, 2021, and references therein). Secondly, many geodynamic simulations incorporate horizontal motions  
65 of the lithosphere, which limits their use as a comparator.

From an observational perspective, it would be useful to establish rules-of-thumb that quantify sensitivity of surface deflec-  
tions to choices made when predicting them. Many such rules are already well known from analytic and numeric solutions  
of the equations of motion (e.g., Colli et al., 2016; Hager and O’Connell, 1979; Holdt et al., 2022; Lees et al., 2020; Parsons  
70 and Daly, 1983). For instance, a suite of benchmark studies exist that compare predictions from numeric mantle convection  
simulations with analytic solutions (see e.g., Bauer et al., 2019; Kramer et al., 2021; Zhong et al., 2008, and references therein).  
Those papers tend to focus on establishing the fidelity of numeric models. In contrast, our goals are to, first, understand how  
calculated deflections are impacted by the choice of methodology used to solve the equations of motion and, secondly, to  
establish sensitivities to popular assumptions incorporated into simulations. We want to know the extent to which an improved  
75 fit between predictions and observations reflects a more Earth-like density and viscosity structure versus modelling choices.  
Our thesis is that performing all tests in a self-consistent framework, as we do in this study, provides a straightforward way  
to collate insights into the sensitivities of predicted surface deflections and to simplify the comparison of predictions from  
different suites of models.

## 80 1.1 Our Approach and Paper Structure

We start by exploring the consequences of solving the equations of motion numerically, using the TERRA software, and analyt-  
ically, using Ghelichkhan et al. (2021)’s propagator matrix algorithms (see Figure 1 & Supporting Information). We make use  
of the flexibility of numeric approaches by incorporating a variety of assumptions and parameterizations that are not amenable  
to analytic attack (e.g., temperature-dependent viscosity). All numeric simulations presented in this paper were driven by the  
85 plate motion history of Merdith et al. (2021, see Figures 1g–h and S1). The models have a resolution of 60 km at their surface  
(see Supporting Information for details of model setup and execution). We note that they do not directly assimilate information  
about the mantle from tomographic models. Ensuring that numeric simulations are accurate and stable means that compu-  
tational burden is often considerable and hence systematic exploration of parameter space remains challenging. In contrast,  
analytic approaches can yield calculated surface deflections that are (mathematically) accurate, whilst including features such  
90 as radial gravitation, with much less computational cost. Consequently, we make use of propagator matrix techniques to explore



parameter space, examine benchmarks, and reproduce results. We establish the sensitivity of solutions to different parameterizations and approaches to solving the equations of motion.

There are at least two important considerations when solving the equations of motion analytically. First, solutions are only known to exist in the spherical harmonic domain for fluid bodies with radial viscosity (i.e., no lateral variability in viscosity). Second, generating solutions in the spherical harmonic domain places practical limits on spatial resolution of solutions. Consider that the number of spherical harmonic coefficients per degree =  $2l + 1$ , where  $l$  is degree, so for a given maximum degree  $L$ , there are  $(L + 1)^2$  coefficients in total. For instance, when  $L = 50$  there are 2,601 coefficients for each model. Consider also that spatial resolution increases approximately with the reciprocal of  $l$  (see Section 2.2). Incorporating all of the output from the numeric models (60 km at the surface) would require  $L \approx 880$ , with 776,161 coefficients, which is computationally cumbersome. Furthermore, observational constraints on mantle-related surface deflection are unlikely to be finer than the flexural wavelength of the overlying lithosphere,  $l \approx 50$  (e.g., Holdt et al., 2022). With these limitations in mind, we compared surface deflections predicted using different approaches at the same resolution up to  $l = 50$  (see Supporting Information and Section 2.3).

105

Most of the tests in this paper compare surface deflections calculated using the entirety of the model domains (i.e., from CMB to the surface). This approach simplifies like-for-like comparisons of model predictions and comparisons to increasingly complex scenarios. However, amplitudes of calculated deflections will of course not reflect estimated amplitudes of dynamic topography. This approach purposefully avoids isolating passive or plate-driven surface deflections and sub-plate support from numeric simulations or analytic solutions. Since the central focus of this work is merely on quantifying contrasts that arise from choices made when simulating mantle convection, we wish to avoid incorporating additional modifications where possible. In subsequent tests we examine the consequences of simply removing shallow structure, a widely used approach for estimating dynamic support from simulations (see e.g., Flament et al., 2013; Wang et al., 2022).

115

With this framework in place we generate, compare and contrast predicted surface deflections. The first suite of tests are purposefully simple, e.g., incompressible, constant gravitational acceleration (no self-gravitation or radial variation in gravitation) and have radial viscosity independent of temperature. Results are compared to estimates of sub-plate support from oceanic age-depth residuals with a view to quantifying corrections necessary to convert predicted instantaneous surface deflections into estimates of sub-plate support. We then systematically examine the impact of incorporating radial variations in gravitational acceleration, contribution to flow from deflection of the gravitational potential field, removal of shallow density structure, choice of surface and CMB slip conditions, inclusion of temperature-dependent viscosity, and amplification or reduction of viscosity and density anomalies in the upper and lower mantle (Section 4; Tables 1–2). A closed-loop modelling strategy is explored in which predicted surface deflections from these relatively complex models are compared to results from simpler reference models. Finally, a methodology for assessing effective contributions to surface topography from mantle anomalies is presented.

125





## 2 Numeric and Analytic Calculations of Surface Deflection

The Supporting Information document summarises the formulations of Stokes' equations that are solved, model parameter values used and the numeric approach to calculating mantle convection using the TERRA finite-element software. Here, we move straight to explaining how those simulations are used to calculate radial stresses,  $\sigma_{rr}$ , thence vertical deflections,  $h$ , at Earth's surface (Figure 1). A methodology for representing model predictions in the spherical harmonic domain is then described. We then examine analytic solutions obtained using propagator matrix techniques.

### 2.1 Deflections calculated using radial stresses from numeric simulation

Following Parsons and Daly (1983), surface deformation is estimated from numeric simulations of mantle convection by making use of the requirement that normal stress is continuous across the upper boundary of the solid Earth (see also McKenzie, 1977; Ricard, 2015). In other words, radial stresses generated by the solid Earth are required to be balanced by stresses generated by the overlying (oceanic or atmospheric) fluid. There are three contributions to normal stress at this boundary from the mantle: hydrostatic stress that would exist even in the absence of convection, dynamic stress arising from convection, and viscous stress which opposes fluid motion (see Equations S2–S6 in Supporting Information). To satisfy the continuity condition, these stresses must be balanced by those generated by the water (or air) column atop this boundary. If the pressure from the overlying column is hydrostatic, the resultant condition is

$$\rho_w g_s h = \rho_m g_s h + \sigma_{rr}, \quad (1)$$

where  $\sigma_{rr}$  incorporates deviatoric viscous stresses generated by mantle convection and dynamic pressure ( $\sigma_{rr} = \tau_{rr} - p$ ), obtained by solving Equation S2 in Supporting Information. In practice, since values for this term are obtained by subtracting radial lithostatic stress from the total stress, values of  $\sigma_{rr}$  integrate to zero globally.  $g_s$  is gravitational acceleration at Earth's surface,  $\rho_m$  is the mean density for the surficial layer, and  $\rho_w$  is the density of the overlying fluid (see Table S1). Note that we do not impose additional oceanic plate cooling, e.g., due to hydrothermal circulation at ridges. Cooling and subsequent subsidence, as well as passive return flow at ridges, arise naturally from solution of the governing equations laid out in Section S2 of Supporting Information.

Surface deflection arising in response to predicted convective flow,  $h$ , is approximated by rearranging Equation 1,

$$h \approx -\frac{\sigma_{rr}}{(\rho_m - \rho_w)g_s}. \quad (2)$$

Deflections are estimated from radial stresses at times of interest (e.g., the present-day) by re-running one time-step of the TERRA model. During that time-step, a free-slip boundary condition, for which analytic approximations for surface deflection exist, is imposed instead of the plate-slip condition prescribed during the main model run routine (see Section 2.3; Ricard,



155 2015). The numeric models themselves apply a quasi-rigid condition at the surface, whereby flow is driven by estimates of  
real plate velocities (from Merdith et al., 2021), and so the surface layers behave as a series of rigid, laterally mobile plates  
rather than a single rigid shell. We assess the accuracy of modifying boundary conditions in this way by converting calculated  
deflections into the spherical harmonic domain and comparing them to predictions generated using the analytic propagator  
matrix approach. The consistent boundary flux (CBF) method provides an alternative means to accurately calculate normal  
160 stresses (Zhong et al., 1993). Previous benchmarking with TERRA has shown mean errors of a few percent or less for surface  
deflection predictions at low harmonic degrees,  $l \leq 16$  (Davies et al., 2013).

## 2.2 Surface Deflections Calculated in the Spherical Harmonic Domain

Transforming stress, or surface deflections, calculated using numeric approaches into the frequency domain provides straight-  
165 forward means of comparing results to analytic solutions and of quantifying spectral power, i.e., the magnitude of contribution  
to the total signal from different wavelengths. Since the models that we investigate are global in scope, we do so using spherical  
harmonics. The methodology for calculating spherical harmonics and the definition of power adopted in this study are included  
as Supporting Information. Figure 2 shows an example of surface stresses calculated using the TERRA code, their spherical  
harmonic representation, calculated surface deflections in the spherical harmonic domain, and associated statistics and power  
170 spectra.

Using the total power per degree convention, Hoggard et al. (2016) derived a rule-of-thumb for estimating the power spec-  
trum of dynamic topography (see their Supporting Information),  $P_l^{DT}$ , using Kaula (1963)'s approximation for the long-  
wavelength gravity field of Earth as a function of  $l$ :

$$175 P_l^{DT} \approx \left( \frac{GM}{ZR^2} \right)^2 \left( \frac{2}{l} - \frac{3}{l^2} + \frac{1}{l^4} \right), \quad (3)$$

where  $G$  is the gravitational constant,  $M = 5.97 \times 10^{24}$  kg is the mass of the Earth,  $R \approx 6370$  km is Earth's radius. The value  
of low-degree admittance,  $Z$ , between gravity and topography varies as a function of viscosity, as well as the depth and wave-  
length of internal density anomalies (Colli et al., 2016). Hoggard et al. (2016) found that assuming an average value of  $Z = 12$   
mGal km<sup>-1</sup> provides a reasonable approximation of observed residual topographic trends, thus we make use of that value in  
180 the remainder of the paper. Finally, it is useful to note that Jeans (1923) related spherical harmonic degree to wavelength  $\lambda$ ,  
which at Earth's surface can be approximated via  $\lambda \approx 2\pi R / \sqrt{l(l+1)}$ .

## 2.3 Surface Deflections Calculated Analytically

The second methodology used to calculate surface deflection in response to mantle convection is the analytic propagator matrix  
185 technique (e.g., Craig and McKenzie, 1987; Gantmacher, 1959; Ghelichkhan et al., 2021; Parsons and Daly, 1983; Richards



and Hager, 1984). The approach we take stems from the work of Hager and O'Connell (1981) who used Green's functions to solve the equations of motion in the spherical harmonic domain. Those solutions are used to generate sensitivity kernels that straightforwardly relate, for example, density or temperature anomalies in the mantle to surface deflections. The kernels are generated in the frequency domain, and constructed such that surface deflection sensitivity to mantle (e.g., density) anomalies is calculated as a function of depth (or radius) and wavenumber. A global spherical harmonic implementation introduced by Hager et al. (1985) has been extended to include compressibility, the effect of warping of the gravitational potential by subsurface density distributions, and radial gravity variations calculated using radial mean density values (Corrieu et al., 1995; Forte and Peltier, 1991; Hager and O'Connell, 1981; Richards and Hager, 1984; Thoraval et al., 1994).

195 In this study, following Ghelichkhan et al. (2021), surface deflection for each spherical harmonic coefficient,  $h_{lm}$ , is calculated in the spectral domain such that

$$h_{lm} = \frac{1}{(\rho_m - \rho_w)} \int_{R_{\text{CMB}}}^R A_l \delta \rho_{lm}(r) \cdot dr. \quad (4)$$

Products of the sensitivity kernel,  $A_l$ , and density anomalies,  $\delta \rho_{lm}$ , of spherical harmonic degree,  $l$ , and order,  $m$ , are integrated with respect to radius,  $r$ , between the core-mantle boundary and Earth's surface radii,  $R_{\text{CMB}}$  and  $R$ , respectively. The sensitivity kernel is given by

$$A_l = - \left( \frac{\eta_0}{Rg_R} \right) \left( u_1 + \frac{\rho_w}{\rho_0} u_3 \right), \quad (5)$$

where  $u_n(r)$  represents a set of poloidal variables, which are posed for solution of the set of simultaneous equations by matrix manipulation, such that

$$u(r) = \left[ y_1 \eta_0 \quad y_2 \eta_0 \Lambda \quad (y_3 + \bar{\rho}(r) y_5) r \quad y_4 r \Lambda \quad y_5 r \rho_0 \Lambda \quad y_6 r^2 \rho_0 \right]^T, \quad (6)$$

205 where  $\Lambda = \sqrt{l(l+1)}$ , and  $y_1$  to  $y_6$  represent the spherical harmonic coefficients of radial velocity  $v_r$ , lateral velocity  $v_{\theta,\phi}$ , radial stress  $\sigma_{rr}$ , lateral stress  $\sigma_{r\theta,\phi}$ , gravitational potential  $V$ , and gravitational potential gradient  $\partial V/\partial r$ , respectively (Hager and Clayton, 1989; Panasyuk et al., 1996).  $\bar{\rho}$  is the layer mean ( $l=0$ ) density. The kernel  $A_l$  includes both  $u_1$  and  $u_3$ , two terms in the matrix solution to the governing equations that affect surface topography by directly exerting stress on the surface boundary ( $u_1$ ), and by changing the gravitational potential at the surface ( $u_3$ ). The functional forms of calculated sensitivity kernels depend on chosen radial viscosity profiles and boundary conditions (e.g., free-slip or no-slip; Parsons and Daly, 1983).

210



### 3 Spatial and Spectral Comparison of Model Predictions

To quantify impacts of modelling assumptions and approaches used to solve the equations of motion we compare calculated surface deflections using the following metrics.

#### 3.1 Euclidean Comparisons of Amplitudes

215 First, we calculate root-mean-squared difference,  $\chi$ , between predicted surface deflections in the spatial domain,

$$\chi = \sqrt{\frac{1}{N} \sum_{n=1}^N w_{\phi} (h_n^a - h_n^b)^2}, \quad (7)$$

where  $h_n^a$  and  $h_n^b$  are predicted surface deflections from the two models being compared.  $N$  = number of points in the  $1 \times 1^\circ$  gridded maps being compared (e.g., Figure 3b;  $N = 65341$ ). The prefactor  $w_{\phi}$  is proportional to  $\cos \phi$ , where  $\phi$  is latitude, and is included to correct biases in cell size with latitude; mean  $w_{\phi} = 1$ . This metric is closely associated with the mean vertical  
220 distance ( $L^2$ -norm distance) between predicted and reference surfaces, i.e.,  $\Delta \bar{h} = 1/N \sum_{n=1}^N w_{\phi} |h_n^a - h_n^b|$ . These metrics are sensitive to differences in amplitudes and locations of surface deflections.

#### 3.2 Spectral Correlation Coefficients

Second, we use pyshtools v4.10 to compute correlation coefficients,  $r_l$ , between predicted surface deflections in the spectral domain (Wieczorek and Meschede, 2018). Correlation coefficients as a function of degree  $l$ , adapted from Forte (2007), are  
225 calculated such that

$$r_l = \frac{\sum f_1^* f_2}{\sqrt{\sum f_1^* f_1} \sqrt{\sum f_2^* f_2}}, \quad \text{where} \quad \sum = \sum_{m=-l}^{+l}, \quad (8)$$

$f_1$  and  $f_2$  are the spherical harmonic coefficients of the two fields (i.e., surface deflections) being compared, which vary as a function of order,  $m$ , and  $l$ ;  $f = f_l^m$ . \* indicates complex conjugation (see also Becker and Boschi, 2002; O'Connell, 1971). This metric is sensitive to the difference between predicted and reference surface deflection signals in the frequency domain,  
230 but not to their amplitudes. To summarize spectral similarity between models concisely, we later refer to the mean value of  $r_l$  over every degree (0–50) as  $\bar{r}_l$ . We refer to the standard deviation of  $r_l$  across degrees as  $s_r$ .

#### 3.3 Comparing Calculated Power Spectra

Lastly, to estimate closeness of fit between power spectra of surface deflections predicted in this study and independent estimates, we calculate



$$235 \quad \chi_p = \sqrt{\frac{1}{L} \sum_{l=1}^L (\log_{10} P_l - \log_{10} P_l^K)^2} + \sqrt{\frac{1}{L} \sum_{l=1}^L (\log_{10} P_l - \log_{10} P_l^H)^2}, \quad (9)$$

where  $L$  = number of spherical harmonic degrees being compared ( $L = 50$ ).  $P_l$  = power of predicted surface deflections generated in this study at degrees  $1 \leq l \leq L$  (Equation S11 in Supporting Information).  $P_l^K$  = power of surface deflections estimated using Kaula's law (Equation 3).  $P_l^H$  = power of residual oceanic age-depth measurements from Holdt et al. (2022).

## 4 Model Parameterizations

240 The models examined in this paper are summarised in Table 1. In terms of assumptions tested there are two families of models, those with viscosity independent of temperature (Models 1–10), and those with temperature-dependent viscosity (Models 11–20). We note that Models 12–20 incorporate mean radial viscosity from the numeric Model 11a in which viscosity depends on temperature. The two approaches used to solve the equations of motion are annotated ‘Numeric’ and ‘Analytic’ in Table 1, which refers to solutions from the TERRA and propagator matrix code, respectively. Viscosities and densities calculated using TERRA were used as input for the propagator matrix code and thus used to generate analytic estimates of surface deflection. Since analytic solutions are obtained by spherical harmonic expansion, surface deflections from TERRA were fit using spherical harmonics before predicted deflections were compared (annotated ‘Mixed’ in Table 1; Section 2.2). We compare predicted deflections that arise from flow across entire model domains, i.e., from the CMB to the surface. Parameterizations of these models and resultant surface deflections are discussed in the following sections, with summary statistics given in Table 2.

### 4.1 Models with Viscosity Independent of Temperature

#### 4.1.1 Reference models

255 Models 1 and 2 are the simplest explored in this paper. They were designed to be as similar as possible, with a view to quantifying differences and similarities arising solely from the choice of numeric or analytic methodology used to solve equations of motion and to calculate surface deflections. Model 1 was parameterized with the radial viscosity structure shown in Figure 2c. Radial viscosity used in other geodynamic studies are shown alongside for comparison (Ghelichkhan et al., 2021; Mitrovica and Forte, 2004; Steinberger and Calderwood, 2006). Figure 2d shows spherical harmonic expansion of the surface stress field predicted by Model 1 at 0 Ma (cf. Figure 2a). We call this result Model 1b. The original, full-resolution, numerical result is referred to as Model 1a.

Model 2 is the analytic model parameterized to be as similar as possible to Model 1. Its sensitivity kernel, generated assuming water loading ( $\rho_w = 1030 \text{ kg/m}^3$ ), free-slip surface and CMB boundary conditions, and the radial viscosity profile shown in



**Table 1. Summary of mantle convection simulations.** Column labeled ‘Method’ indicates surface deflections calculated using either ‘*Numeric*’ (i.e., from surface normal stresses calculated using TERRA) or ‘*Analytic*’ (i.e., propagator matrix) approaches; ‘*Mixed*’ indicates spherical harmonic fitting of surface stresses calculated using numeric code, enabling comparison with solutions to propagator matrix code.  $\eta(r)$  indicates models with radial viscosity (e.g. independent of temperature; Models 1–10).  $\eta(r, T)$  indicates models with temperature-dependent (therefore laterally varying) viscosity (Models 11–20); note that analytic Models 12–20 incorporate radial viscosity calculated using mean radial viscosity from Model 11a. <sup>†</sup> indicates with respect to Model 12. See Table 1, Section 4 and figures referred to in column 5 for details.

Model	Method	Viscosity	Parameterizations	Figures
1a	Numeric	$\eta(r)$	Unfiltered numeric model	1g-h, 2a-c, S1-2
1b	Mixed	$\eta(r)$	Spherical harmonic fit to 1a	2d-i
2	Analytic	$\eta(r)$	Propagator matrix solutions	3, S3
3	Analytic	$\eta(r)$	Radial gravitation, $g(r)$	4a-c, S4
4	Analytic	$\eta(r)$	Gravitational potential terms	4d-e, S5
5	Analytic	$\eta(r)$	Removing upper 50 km of mantle	5a-b, S7a-d
6	Analytic	$\eta(r)$	Removing upper 100 km of mantle	5c-d, S7e-h
7	Analytic	$\eta(r)$	Removing upper 200 km of mantle	5e-f, S7i-l
8	Analytic	$\eta(r)$	No-slip surface, free CMB	6a-d
9	Analytic	$\eta(r)$	Free surface, no-slip CMB	6e-h
10	Analytic	$\eta(r)$	No-slip surface, no-slip CMB	6i-l
11a	Numeric	$\eta(r, T)$	Unfiltered numeric model	S8-S10, S12a-c
11b	Mixed	$\eta(r, T)$	Spherical harmonic fit to 11a	7, S8-10, S12d-g
12	Analytic	$\eta(r)$	Mean radial $\eta(r, T)$ from Model 11a	7, S11, S12h-k
13	Analytic	$\eta(r)$	Decrease <sup>†</sup> radial upper mantle $\eta$	8a-b, S13a-d
14	Analytic	$\eta(r)$	Increase <sup>†</sup> radial upper mantle $\eta$	8c-d, S13e-h
15	Analytic	$\eta(r)$	Increase <sup>†</sup> radial upper mantle $\eta$	8e-f, S13i-l
16	Analytic	$\eta(r)$	Constant radial $\eta$	8g-h, S13m-p
17	Analytic	$\eta(r)$	Upper mantle densities $\times 2^{\dagger}$	8i, S14a-c
18	Analytic	$\eta(r)$	Upper mantle densities $\times 1/2^{\dagger}$	8j, S14d-f
19	Analytic	$\eta(r)$	Lower mantle densities $\times 2^{\dagger}$	8k, S14g-i
20	Analytic	$\eta(r)$	Lower mantle densities $\times 1/2^{\dagger}$	8l, S14j-l



Figure 2c, is shown in Figure 3a. Values of the other parameters used to generate these kernels are stated in Table S1. Similar to  
 265 many previous studies, the kernel indicates that surface deflections will be especially sensitive (across all degrees incorporated,  
 $l \leq 50$ ) to density anomalies in the upper mantle (Parsons and Daly, 1983; Hager and Clayton, 1989; Ghelichkhan et al., 2021).  
 Models 1 and 2 are used as points of reference for other more complex models explored in the remainder of this paper.

#### 4.1.2 Gravitation

We start by incorporating more complex parameterizations of gravitation. The analytic Model 3 was parameterized in the same  
 270 way as Model 2 with the addition of radial gravitation (following Hager and Clayton, 1989; Panasyuk et al., 1996, see Equation  
 5). The solid curve in Figure 4b shows the radial gravity function used to calculate surface deflections. It was generated using  
 the density distribution produced by (the numerical) Model 1a (see Figure S1) by calculating

$$g(r) = \frac{4\pi G}{r^2} \left[ \int_{R_{\text{CMB}}}^r \bar{\rho}(r') r'^2 dr' \right] + F_{\text{core}}, \quad (10)$$

where  $\bar{\rho}(r)$  is layer mean density and  $F$  is a factor chosen to account for core mass, and such that  $g = 9.8 \text{ m s}^{-2}$  at the sur-  
 275 face. This formulation is derived from Gauss's law assuming spherically symmetric density, combined with Newton's law of  
 universal gravitation (Turcotte and Schubert, 2002).

The analytic Model 4 incorporates stress perturbations induced by deflections of the gravitational potential field. This model  
 assumes  $g = 10 \text{ m s}^{-2}$  everywhere, even within the deflected surface layer, as was the case for Models 1–2. Following Hager  
 280 and Clayton (1989) and Panasyuk et al. (1996), when solving for surface deflection using propagator matrices, the effect on  
 flow of perturbation of gravitational potential is included via the  $u_3$  term in Equation 6 (see also Ribe, 2007; Ricard, 2015).  
 Sensitivity kernels for Models 3 and 4 are shown in Figure S6. TERRA simulations do not include this component in flow  
 calculations (see Supporting Information).

#### 4.1.3 Discarding Shallow Structure

285 The uppermost few hundred kilometers of geodynamic simulations are often not included in predictions of surface deflections  
 (see e.g. Flament et al., 2013; Flament, 2019; Davies et al., 2019, and references therein). To quantify the impact of discarding  
 shallow structure on our calculations, we examine differences in calculated deflections in the spatial and spherical harmonic  
 domains. We present three tests, resulting in Models 5, 6 and 7, where structure shallower than 50, 100 and 200 km is removed  
 from Model 2.

#### 290 4.1.4 Changing Boundary Conditions

Up to now, we have only considered instantaneous analytic and numeric solutions for surface deflection where both the sur-  
 face and CMB have free-slip conditions imposed (i.e., vertical component of flow velocity  $\mathbf{u}_r = 0$ , horizontal components are





allowed to freely vary). No gradient/Neumann constraint (e.g., on  $\partial \mathbf{u} / \partial z$ ) is imposed. This condition is generally deemed appropriate for the surface of the convecting mantle, and CMB, since at both boundaries, cohesion within convecting mantle is thought to be much stronger than adhesion to the boundary. Analytic solutions for sensitivity kernels for propagator matrices also exist for no-slip Dirichlet boundary conditions, where horizontal components of  $\mathbf{u} = 0$ , which may be more appropriate when the Earth's lithosphere is implicitly included in mantle convection models, as is the case here (Parsons and Daly, 1983; Thoraval and Richards, 1997). Therefore, we test the effect of changing the surface boundary condition to no-slip on predicted surface deflections (Model 8). Although there is little reason to believe the adhesion of the CMB would be strong, for completeness, we test scenarios in which no- and free-slip conditions are assumed for the CMB and the surface, respectively (Model 9), and both have no-slip conditions (Model 10).

#### 4.2 Models with Temperature-Dependent Viscosity

We investigate the impact of including the temperature dependence of viscosity,  $\eta(r, T)$ , on predicted global mantle flow in numeric models, and on subsequent estimates of surface deflection. We do so by first generating the numeric Model 11, which is identical to Model 1 in terms of all boundary conditions, initialization, and physical parameters, except for the fact that viscosity depends on temperature in the manner described by Equation S7 in Supporting Information.

The radial distribution of viscosity, but not its absolute value, plays a crucial role in determining sensitivity of instantaneous solutions for surface deflections to density (and thermal) anomalies in the mantle (e.g., Parsons and Daly, 1983; Hager, 1984). Consequently, to assess sensitivity of surface deflections to arbitrary changes to radial viscosity,  $\eta(r)$ , we performed a suite of analytic tests. Since the analytic approaches require viscosity to only vary as a function of radius, we first test the impact of inserting layer-mean viscosity from the present-day 3D temperature-dependent viscosity structure predicted by numeric Model 11 (Figure S8). This parameterization is used to generate (the analytic) Model 12. The sensitivity kernel for Model 12 is shown in Figure S11a.

315

We stress that in Models 3–10 analytic instantaneous solutions for surface deflection, with adjusted parameters and boundary conditions, were simply compared with Model 2; no new numeric models were generated using TERRA. In contrast, the additional tests examined here correspond to a new TERRA model (Model 11) in which temperature dependence of viscosity affects mantle flow across the entire run time.

320

The sensitivity of surface deflections to arbitrary modification of upper and lower mantle viscosity and densities were then examined. Mean upper and lower mantle (radial) temperature-dependent viscosity was decreased or increased by an order of magnitude from that used to generate Model 12 (see solid black curve in Figure 8). The resultant impact on calculated surface deflections (Models 13–16) was quantified by comparison with results generated using reference Model 12 (Figure S11). Figures 8i–l and S14 show the amplitudes of density anomalies in the upper and lower mantle that were systematically increased or decreased to generate Models 17–20. Similar to the tests shown in Figures 8a–h and S13, densities are amplified



relative to Model 12. Radial viscosity is constant for each of these tests (black curve in Figure 8a; i.e., same as that used to generate Model 12).

## 5 Results

### 330 5.1 Models with Viscosity Independent of Temperature

#### 5.1.1 Reference Models: Comparing Numeric and Analytic Solutions

We first compare solutions generated from numeric Model 1a, with its spherical harmonic representation (Model 1b), and analytic Model 2, which were designed to be as similar as possible. Figure 1g–h shows calculated densities that arise in Model 1a at 0 and 100 Ma (see Figure S1 for extended results). The history of plate motions used to drive these models is also indicated  
335 on these figures. The resultant normal stresses,  $\sigma_{rr}$ , calculated at the surface of Model 1, and associated statistics are shown in Figure 2a–b. By convention, positive stresses imply compression and hence downward surface deflection, which could be manifest as lithospheric drawdown, i.e., subsidence. Prominent regions of positive stress anomalies in this model include locations atop imposed collision zones, where subduction naturally results, e.g., along the Pacific margin of South America. Negative stresses imply dilation and hence positive lithospheric support (i.e., surface uplift). Figure 2a shows dilatational stresses be-  
340 neath Southern Africa, for example, and along mid-oceanic ridges in the Indian and Atlantic Oceans.

Surface stresses calculated by fitting radial stresses from Model 1a with a global spherical harmonic interpolation up to maximum degree  $l = 50$ , i.e., minimum wavelength of  $\approx 800$  km, is shown in Figure 2d–e. The resultant power spectrum in terms of total power at each degree is shown in Figure 2f. Aside from the lack of structure at degree 0, amplitudes decrease steadily  
345 with increasing degree (i.e., decreasing wavelength) and can be approximated by red noise. The spherical harmonic representation of deflections calculated by converting stress using Equation 2, assuming water loading, are shown in Figures 2g and S2. A comparison of calculated power spectra, expected surface deflection from Kaula’s rule (Equation 3), and spectra generated from observed residual ocean age-depth measurements is also included in Figures 2 and S2 (Kaula, 1963; Hoggard et al., 2016; Holdt et al., 2022). For completeness, surface deflections calculated assuming air loading are shown in Figure S2f–j.

350

Surface deflections predicted by Model 2 and its associated sensitivity kernel are shown in Figure 3a–b. An expanded set of results including sensitivity kernels for water and air loading, and histograms of deflection and associated power spectra are included in Figure S3.

355 Deflections predicted from these numeric and analytic models are visually similar (cf. Figures 2g & 3b). Absolute differences in amplitudes are greatest close to subduction zones (e.g., in South America and Asia; Figure 3c). The differences are broadly normally distributed and centred on 0 (Figure 3d). The spherical harmonic correlation between these models is high (close to 1 for all degrees; cf. Forte, 2007, Figure 3e). The ratios between surface deflection values in these predictions indicate that



analytic solutions tend to be damped compared to numeric solutions. This result is emphasized by the histogram shown in  
360 Figure 3g. Multiplying amplitudes of deflections from the propagator matrix solutions by a factor of 1.1 brings them in-line  
with the numeric solutions. These results indicate that the propagator matrix approach dampens solutions by  $\approx 10\%$ . We note  
that power spectral slopes between Model 1b and 2 are similar (cf. Figures 2i and S3d). These and all other results are discussed  
in Section 6.

### 5.1.2 Incorporating Self-Gravitation and Gravitational Potential of the Deflected Surface

365 Differences in deflections predicted by Model 2, which assumes constant  $g = 10 \text{ m s}^{-2}$  across all radii, and Model 3, which in-  
corporates self-consistently calculated radial gravitation, are shown in Figure 4a and 4c. Deviations in predicted instantaneous  
deflections are  $\sim 10\%$  of maximum amplitudes predicted by Model 2 (see Table 2). Note that, for the viscosity structure used  
in these models, changing  $g$  in this way impacts sensitivity kernels most at low degrees  $l \lesssim 10$  in the mid-mantle (see Figures  
2c, 3a and S6).

370

We suggest that the broadly hemispherical differences in calculated deflections arise from three contributing factors. First,  
deviations in  $g$  between the two models are greatest in the mid-mantle, which, secondly, results in subtly different sensitivity  
kernels (see Figure S6). In general, surface deflection sensitivity to mid-mantle structure is highest at low degrees ( $l = 1-3$ ), and  
is almost negligible at higher degrees compared to contributions from the near-surface. Thus it seems likely that differences  
375 between these kernels would be manifest in low-degree (e.g. hemispherical) differences in surface deflections. Third, in the  
final timestep, which is used to calculate deflections, there occurs a greater proportion of negative and positive deflections in  
the northern and southern hemispheres, respectively.

We note that incorporating radially varying gravitation into numeric simulations, which is not trivial, might materially im-  
380 pact calculated mantle flow fields and hence predictions of surface deflections (see e.g., Zhong et al., 2008; Liu and King,  
2019). Our results are consistent with the rule of thumb outlined in Section 7.02.2.5.2 of Ricard (2015), whereby magnitudes  
of differences incurred by inclusion of full self-gravitation, i.e.,  $g(\theta, \phi, r)$ , decay as a function of spherical harmonic degree,  
proportionately to  $3/(2l + 1)$ .

385 As expected, induced differences in surface displacement predictions are much lower in magnitude when gravitational  
potential of the deflected surface is included compared to when radial gravitation is incorporated (cf. Figure 4a and 4d).  
We note that they are of the same order of magnitude as the geoid height anomalies predicted by these models. The mean  
Euclidean distance between the two predicted surfaces in Models 2 and 4 is only  $\sim 110 \text{ m}$  (compared to maximum amplitudes  
> 8 km), and the spherical harmonic correlation is very high across all degrees (see Table 2). Similar to the results for Model 3,  
390 the differences are concentrated at low spherical harmonic degree  $l$ . We stress that this test investigates the effect of the  $u_3$  term  
on instantaneous solution for surface deflection (Equation 5). It cannot be ruled out from this test that inclusion of the effect



of gravitational potential field perturbation would result in greater differences across the entire model run time of a numeric model, although it is unlikely (Zhong et al., 2008).

### 5.1.3 Excising Shallow Structure

395 As expected from examination of surface deflection sensitivity kernels (e.g., Figure 3a), removal of shallow structure (Models 4–6) results in significantly reduced amplitudes of surface deflections (Figure 5). Doing so results in amplitudes of power spectra that more closely align with independent estimates (Figure 5b, f, j). The reduction in differences is largely due to the fact that the reference Model 2 has surface deflections that are much larger than independent estimates of dynamic topographic power across all degrees. We note that power spectral slopes for predicted surface deflection from Model 2 are close to those  
400 generated from Kaula’s rule, and observed oceanic residual depths (Figures 2i, S2 and S3). Removing shallow structure steepens spectral slopes (i.e., reduces power at high degrees) beyond those expected from theoretical considerations (Kaula’s rule) or observed from oceanic residual depths, akin to results from other work that excised shallow structure (e.g., Flament et al., 2013; Moucha et al., 2008; Steinberger, 2007). This result is emphasized by calculated spectral coherence,  $r_l$ , between deflections with and without shallow structure removed (cf. Figure 5b, d, f). While degree 1 and 2 structure remains coherent, coherence  
405 across degrees  $\gtrsim 20$  decreases from  $\sim 0.9$  to as low as 0.5, which are the largest discrepancies between any models examined in this study (Figure S7).

### 5.1.4 Adjusting Boundary Conditions

Figure 6a, e and i show predicted sensitivity kernels as a function of depth and degree, for no-slip/free-slip, free-slip/no-slip and no-slip/no-slip boundaries respectively, where the first condition is the surface slip condition, and the second the CMB slip  
410 condition. Differences to the sensitivity kernel for Model 2 (free-slip/free-slip; Figure 3a) are shown in panels b, f and j. Those panels, and panels c, g and k, demonstrate that when the surface boundary condition is ‘no-slip’, there is decreased sensitivity to short wavelength shallow structure, and increased sensitivity to long-wavelength (low degree) structure across all depths. Figure 6d, h and l reveal that induced misfit in the spatial domain is impacted to a greater degree than in tests of gravitation (Models 3 & 4), but not necessarily more severely than for removal of, say the upper 200 km of density structure from surface  
415 deflection calculations. Spectral correlation with Model 2 is most severely impacted when both surface and CMB boundaries are no-slip, which is probably physically unrealistic (Model 7; see Table 2; Section 4.1.4).

## 5.2 Adjusting Viscosity and Density Anomaly Amplitudes

### 5.2.1 Temperature-Dependent Viscosity

Slices through the three-dimensional viscosity and density structure of Model 11, which incorporated temperature-dependent  
420 viscosity, are shown in Figure 1a, c and e. Density anomalies in the models parameterized with temperature-dependent viscosity are more localised (‘sharper’) than in the models with viscosity independent of temperature (e.g., Model 1; see Figures 7 & S8–S10). This result is unsurprising since temperature-dependent viscosity provides stronger mechanical contrasts between



cooler subducting regions and surrounding asthenosphere (cf. Figure 1g–h & S9; Zhong et al., 2000). Nonetheless, power spectra of calculated surface deflections are very similar (cf. Figure S10j & 2i). This result emphasises the relatively small  
425 impact incorporating temperature-dependent viscosity has on surface deflections compared to, say, excising shallow structure.

Calculated power spectra from the analytic Model 12, which was generated using layer-mean (radial) viscosity from Model 11a, reinforces this view (cf. Figure S3a-d & Figure S11a-d). Similar to the results obtained for models without temperature-dependent viscosity (Figure 3), deflections calculated analytically are damped relative to numeric solutions (see Figure 7f). The  
430 best fit amplification factor to align propagator matrix and numeric solutions is 1.24 (24%). The effect is greater than that seen when comparing Models 1b and 2 because of increased short wavelength structure in Model 11 (see also Zhong et al., 2000). Nonetheless, spherical harmonic correlations,  $r_l$ , are  $> 0.75$  for all degrees examined ( $l \leq 50$ ), and  $> 0.85$  for most degrees. Cell-to-cell differences in surface deflections are broadly normally distributed and centred on zero (Figure 7d).

435 A summary of comparisons between models with and without temperature-dependent viscosity is shown in Figure S12. Discrepancies in cell-to-cell deflections are broadly normally distributed and centred on zero, clustering along the 1:1 relationship with maximum  $\chi = 1.51$  for unfiltered (numeric) models (Figure S12b-c; see Table 2). Unsurprisingly, spherical harmonic fits and analytic results have tighter normal distributions and lower  $\chi$  values. Correlation coefficients are  $> 0.75$  for nearly all degrees in all comparisons.

## 440 5.2.2 Sensitivity to Upper/Lower Mantle Viscosity and Density Anomalies

In order to explore the consequences of modified viscosity and density on calculated deflections we also systematically increased and decreased contrasts in the upper and lower mantle (Models 13–20) with respect to Model 12. Figure 8 summarises the results, which include decreasing upper mantle viscosity by an order of magnitude and show the impact of using increasingly simple radial viscosity in analytic calculations. Calculated sensitivity kernels for the adjusted viscosity profiles demonstrate that decreasing upper mantle viscosity reduces sensitivity of surface deflections to long-wavelength density structure,  
445 especially in the lower mantle (Figures S13 & 8d, f, h). Models 13–16 have broad similarities with the reference Model 12 even when  $\eta(r)$  is drastically varied: average  $\chi$  misfit = 0.17–0.38 km, and  $r_l > 0.97$  across all degrees. These results emphasize that the viscosity adjustments we examined exert a relatively minor control on the amplitudes of instantaneous surface deflection (Table 2, see, e.g., Ghosh et al., 2010; Moucha et al., 2007; Lu et al., 2020).

450

In contrast, increasing (Model 17) or decreasing (Model 18) upper mantle densities is much more impactful on amplitudes of calculated surface deflections (see Figure 8i–l, and S14). For instance, increasing or decreasing upper mantle densities by a factor of two (relative to Model 12) results in  $\chi$  values of 0.97 and 0.48, respectively. Modifying lower mantle densities has a much smaller impact on amplitudes of deflection (Models 18 & 19). Spherical harmonic correlation between models is approximately as good as for the radial viscosity tests (Models 13–16), which is to be expected since we do not vary locations of  
455 density anomalies here, only their amplitudes, and  $r_l$  is insensitive to amplitudes of the two results being compared. Significant



is the fact that mean vertical differences between Models 17–20 and 12 (i.e.,  $\chi$  and  $\Delta\bar{h}$ ) are higher than those calculated for Models 13–16 (in which viscosity is varied; see Table 2).

460 These results emphasize the relative sensitivity of instantaneous surface deflections to upper mantle density anomalies compared to, say, radial viscosity or lower mantle densities. Even quite large uncertainties in lower mantle density anomalies have relatively little impact on instantaneous surface deflections. These results reinforce the view that accounting for shallow (e.g., lithospheric and asthenospheric) densities is crucial when estimating surface deflection, and dynamic topography, from mantle convection simulations (e.g., Colli et al., 2016; Flament et al., 2013; Holdt et al., 2022; Wang et al., 2022).

465

## 6 Discussion

### 6.1 Similarities of Analytic and Numeric Solutions

In this paper we compare numeric and analytic predictions of instantaneous surface deflections generated by mantle convection simulations. First, we simply compared predictions from numeric and analytic approaches parameterised to be as similar as possible. In this test, the models were purposefully simple: viscosity is radial, models are incompressible, and they do not include self-gravitation, or radial variation in  $g$ . Numeric solutions were transformed into the frequency (spherical harmonic) domain so that they could be compared with analytic solutions, and so that power spectra could be directly compared at appropriate scales. The results show that, for as-similar-as-possible parameterizations, amplitudes of analytic solutions are  $\approx 10\%$  lower than numeric solutions (Figure 3). If the numeric model incorporates temperature-dependent viscosity, this discrepancy increases to 25% (Figure 7). We interpret these results in two ways. First, once armed with viscosity and density fields, numeric and analytic approaches broadly yield similar estimates of surface deflections. Second, the relatively damped analytic solutions are a consequence of smoothing steps in the propagator matrix approach.

The smoothness of analytic solutions, and subsequent damping of topographic amplitudes, is perhaps surprising, given the fact that they are being compared with numeric models expanded into the spherical harmonic domain to the same maximum degree,  $l = 50$ . However, the surface stresses used to generate Model 1a have full horizontal resolution ( $\approx 45$  km) across depths, and *only* the surface layer is smoothed by spherical harmonic fitting, to generate Model 1b. Therefore, Model 1b inherently contains some contribution from degrees  $\geq 50$ , in the sense that finer-resolution density structure at depth could affect longer-wavelength flow nearer the surface. In contrast, to generate the analytic solution (Model 2), the density structure of each layer of the model is smoothed, by expansion to maximum  $l = 50$ , *before* integration of their contributions to surface deflection. The analytic solution would provide a better match to stress estimates from numeric models if such estimates were calculated using density structure smoothed to the same maximum  $l$  across all depths, which is currently challenging (see Section 1.1).

485



**Table 2. Inter-model comparison of predicted surface deflections.** Models being compared are summarised in Table 1. Metrics: root-mean-squared difference ( $\chi$ , km), mean Euclidean ( $L^2$ -norm) difference in predicted deflection ( $\Delta\bar{h}$ , km), and mean spherical harmonic correlation between models ( $\bar{r}_l$ ). Standard deviation of  $r_l$  distribution across degrees ( $s_r$ ) is also stated: note that  $r_l \leq 1$ . All spherical harmonic representations of output from numeric code and generated by the propagator matrix code are expanded up to maximum degree,  $l = 50$ . See body text, figures referred to in column 6, and Table 1 for details.

Models	$\chi$	$\Delta\bar{h}$	$\bar{r}_l$	$s_r$	Figures
1b & 2	0.95	0.69	0.97	0.02	3
2 & 3	0.57	0.47	0.99	$4 \times 10^{-4}$	4
2 & 4	0.13	0.11	0.99	$2 \times 10^{-5}$	4
2 & 5	0.67	0.48	0.93	0.04	5a-b
2 & 6	1.03	0.74	0.87	0.06	5c-d
2 & 7	1.57	1.12	0.63	0.15	5e-f
2 & 8	1.26	1.04	0.99	$1 \times 10^{-3}$	6a-d
2 & 9	1.09	0.97	0.99	0.04	6e-h
2 & 10	1.00	0.74	0.96	0.28	6i-l
1a & 11a	1.51	1.04	—	—	S12a-c
1b & 11b	1.44	0.98	0.79	0.26	S12d-g
11b & 12	1.20	0.80	0.95	0.02	7
2 & 12	0.92	0.64	0.85	0.27	S12h-k
12 & 13	0.31	0.20	0.99	$9 \times 10^{-3}$	8a-b, S13a-d
12 & 14	0.17	0.10	0.99	$3 \times 10^{-3}$	8c-d, S13e-h
12 & 15	0.32	0.20	0.98	0.01	8e-f, S13i-l
12 & 16	0.38	0.23	0.98	0.01	8g-h, S13m-p
12 & 17	0.97	0.64	0.98	$7 \times 10^{-3}$	8i, S14a-c
12 & 18	0.48	0.32	0.98	$6 \times 10^{-3}$	8j, S14d-f
12 & 19	0.43	0.29	0.99	$3 \times 10^{-3}$	8k, S14g-i
12 & 20	0.22	0.14	0.99	$1 \times 10^{-3}$	8l, S14j-l





Nonetheless, the similarity of results indicates that the relatively low-cost propagator matrix approach can be used to explore  
490 consequences of including additional model complexity. A systematic sweep of parameters, including radial gravitation (Fig-  
ure 4a-c) and gravitational potential field effects (Figure 4d-e) indicates that their effects on surface deflection are relatively  
modest. A useful rule of thumb is that self-gravitation perturbs instantaneous surface deflections by  $O(1-10)\%$  when compared  
to models with constant gravitational acceleration, and even less difference is observed at high degree (e.g., Ricard, 2015,  
their Section 7.02.2.5.2). Incorporating the effect of deflections of gravitational potential field on flow has a modest impact on  
495 amplitudes of surface deflections at degrees 1–2, but overall it contributes even less than radial variation in  $g$  to surface de-  
flections across the scales of interest. We note that incorporating full 3-D self-gravitation into numeric simulations is currently  
challenging. Nonetheless, establishing its impact on the flow field over time, and resultant impact on surface deflections, may  
be important future work.

## 6.2 Importance of Viscosity and Shallow Density Anomalies for Isolating Dynamic Support

500 Figure 8 demonstrates that even quite large (order of magnitude) variations in viscosity do not have much impact on instan-  
taneous surface deflections when compared to, say, modified upper mantle density anomalies, which appears to agree with  
the results of Davies et al. (2019) (see also Flament, 2019; Steinberger et al., 2019). Assuming no-slip boundary conditions  
at Earth’s surface may be appropriate for driving near-surface (lithospheric) flow throughout the main model run time, but it  
is less clear whether no- or free-slip boundary conditions are most appropriate for calculating instantaneous dynamic topography  
505 (see, e.g., Forte and Peltier, 1994; Thoraval and Richards, 1997). Nonetheless, all calculated sensitivity kernels in this study  
indicate that shallow density anomalies make significant contributions to surface topography regardless of viscosity profile or  
boundary conditions chosen (e.g., Figure 3a; see also Colli et al., 2016; Parsons and Daly, 1983).

It is well known that disentangling contributions to Earth’s surface topography from mantle convection, lithospheric isostasy  
510 and flexure is important but not trivial (see, e.g., Davies et al., 2019; Cao and Liu, 2021; Fernandes and Roberts, 2021; Hoggard  
et al., 2021; Steinberger, 2016; Stephenson et al., 2021; Zhou and Liu, 2019; Wang et al., 2022). Previous studies simulating  
mantle convection have addressed this issue by discarding density anomalies in radial shells shallower than specified depths  
before calculating surface stresses (e.g., Spasojevic and Gurnis, 2012; Flament et al., 2013; Molnar et al., 2015). Similarly, an-  
alytic approaches have isolated contributions from the convecting mantle by only incorporating information from deep shells  
515 (e.g., Colli et al., 2018). This method has the advantage of effectively removing the effect of lithospheric cooling through  
time from surface deflection estimates. It also avoids the need to incorporate, say, realistic crustal or depleted lithospheric lay-  
ers within the viscous flow parameterization. However, uncertain oceanic and continental lithospheric thicknesses mean that  
choosing appropriate cut-off depths is not simple.

520 Out of all the tests performed in this study, removing shallow structure resulted in the largest impact on predicted surface  
deflections. It modifies amplitudes of deflections, locations of uplift and subsidence, and degrees over which they are resolved,  
and hence modifies power spectral scalings (Table 2, Figure 5). Making quantitative predictions of dynamic topography from



such an approach is fraught for at least two reasons. First, if the chosen depth is shallower than the lithosphere-asthenosphere boundary in places, plate and sub-plate contributions to topography will be entangled. Second, discarding deeper layers to ensure that all plate contribution is definitely avoided means that some contributions from asthenospheric flow will be missed. Thus, such a step is unlikely to be desirable if mantle flow models are to be used to understand, say, lithospheric vertical motions, or vice versa (see e.g., Figure 3a; Davies et al., 2019; Hoggard et al., 2016). Given the calculated sensitivity kernels, excising layers in the upper few 100 km is likely to result in predictions of surface deflections that are especially inaccurate at short wavelengths, i.e., high spherical harmonic degree. An alternative approach, which may be fruitful future work, is removal of structure based on appropriately calibrated plate models, or globally averaged age-dependent density trends (e.g., Richards et al., 2020, 2023).

### 6.3 Assessing ‘Effective’ Contributions to Instantaneous Deflections

The results emphasise the importance of considering sensitivities of instantaneous vertical surface deflections to the location and scale of flow in the mantle. Taking inspiration from Hager and O’Connell (1981) and Parsons and Daly (1983), we calculate the net contributions from density anomaly structure to deflections, as a function of radius, latitude and longitude across all spherical harmonic degrees considered (i.e.,  $l = 1$  to 50). Contributions to deflections from densities at particular radii  $r$ , across all spherical harmonic degrees and orders, for each latitude and longitude,  $(\theta, \phi)$ , are calculated such that

$$h_e(\theta, \phi, r) = \sum_{l=1}^L \sum_{m=-l}^{m=l} [Y_{lm}(\theta, \phi) \cdot \delta\rho_{lm}(r) \cdot A_l(r) \cdot \Delta r], \quad (11)$$

where  $\Delta r$  is the radial width of the spherical shell included in the calculation ( $\approx 45$  km for all shells from the surface to the CMB; see Supporting Information) and  $Y_{lm}$  are spherical harmonic coefficients. Mean density anomalies,  $\delta\rho_{lm}$ , within each shell at each latitude and longitude, and sensitivities  $A_l$  at the top of each shell are used to calculate  $h_e$  (see Section 2.3). Contributions at specific locations to surface deflections as a function of latitude and longitude, and spherical shell depth are shown in Figure 9 for Model 12, for  $1 \leq l \leq 50$ . Results for lower maximum degrees are shown in Supporting Information. Panels a-d show slices through effective density in the upper (at 45, 135, 360 km) and lower mantle (1445 km). A 180° cross-section showing effective densities from the core-mantle-boundary to the surface beneath the Pacific to the Indian Ocean encompassing South America and southern Africa (the same transect as shown in Figure 1) is shown in panel e. This figure again emphasizes the contribution of density anomalies in the upper mantle to surface deflections, and the risks associated with discarding shallow structure when predicting dynamic topography.

### 6.4 Summary and Future Work

Encouragingly, although predicted instantaneous surface deflections are sensitive to different parameterizations, broadly coherent patterns emerge in all models tested. Moreover, calculated deflections are relatively insensitive to the methodologies used to solve the equations of motion. For instance, incorporation of gravitational potential of deflected surfaces, self-gravitation and



viscosity anomalies each generate subtly different surface deflections. Choosing to solve the equations of motion analytically or numerically changes calculated deflections by  $< 25\%$ , even when temperature-dependent viscosity is included throughout  
555 the duration of a simulation.

In contrast, removal of shallow structure produces much larger discrepancies between predicted deflections. For instance, surface deflections calculated using the entire modelling domain (core-mantle boundary to surface) have spectral slopes consistent with those of oceanic age-depth residuals, however amplitudes are over-predicted by 1–2 orders of magnitude. In contrast,  
560 by not including the shallowest 200 km, calculated power spectra more closely match observed amplitudes, especially at spherical harmonic degrees  $> 10$  (Figure 5). However, the spectral slopes of predicted deflections are redder than for the oceanic residuals, which implies that a different approach to removing the contribution of lithospheric structure is required.

An obvious necessary next step for accurately predicting modern dynamic support from mantle convection simulations is  
565 to incorporate accurate information about lithospheric structure from, for instance, tomographic models (e.g., Priestley and McKenzie, 2013; Richards et al., 2020). Another useful next step is to establish sensitivity of surface deflections to time-dependent parameters that impact predicted flow histories, including plate motions. The results in this paper indicate that comparing predicted and observed surface deflections, combined with knowledge of lithospheric structure, could be used to identify optimal models.

570

Finally, the body of geologic and geomorphologic observations that could be used to test predicted histories of surface deflections from mantle convection simulations has grown substantially in the last decade (e.g., uplift and subsidence histories; Section 1; see, e.g., Hoggard et al., 2021, and references therein). A suite of other geologic and geophysical observables are also predicted by, or can be derived from, such simulations (e.g., mantle temperatures, heat flux, geoid, seismic velocities,  
575 true polar wander). Using them alongside histories of surface deflections to identify optimal simulations is an obvious avenue for future work (e.g., Ball et al., 2021; Lau et al., 2017; Panton et al., 2023; Richards et al., 2023). Using such data and the methodologies explored in this paper may be a fruitful way of identifying optimal simulations from the considerable inventory that already exists.

## 7 Conclusions

580 This study is concerned with quantifying sensitivities and uncertainties of Earth's surface deflections that arise in simulations of mantle convection. Calculated sensitivities of instantaneous deflection of Earth's surface to mantle density structure emphasise the importance of accurate mapping of the upper mantle. Surface deflections are somewhat sensitive to the distribution of viscosity throughout the mantle, but especially to the locations and scales of density anomalies in the upper mantle. The largest discrepancies between predicted deflections seen in this study are generated when upper mantle structure is excised  
585 or altered. Doing so changes both the amplitude and distribution of calculated deflections, modifying their power spectral



slopes. These results emphasise the importance of incorporating accurate models of lithospheric structure into calculation of sub-plate support of topography, and also the need to accurately determine plate contributions to topography. In contrast, the choice of methodology to estimate surface deflections—analytic or numeric—or boundary conditions are relatively small sources of uncertainty. Similarly, assumed gravitational profiles and temperature dependence of viscosity are relatively minor contributors to uncertainty given reasonable, Earth-like, parameterizations. Nonetheless, these parameterizations may impact surface deflections through their role in determining how upper mantle flow evolves through geologic time. A fruitful next step could be to use the approaches developed in this paper, in combination with careful isolation of plate cooling signatures from surface deflection predictions, to test mantle convection simulations using the existing and growing body of geologic, geomorphologic and geophysical observations.

595 *Code availability.* TERRA models are archived [here]. The propagator matrix code is archived [here]. Parameterization files are archived [here]. [TO ED: this section will be completed upon final submission, when confirmation of the precise models published is obtained after review.]

*Author contributions.* Conceptualization: GR. Formal analysis: CO, VF, JP. Funding acquisition: GR, HD. Investigation: COM, GR, JP, FR, HD, VF, SG. Methodology: COM, GR, HD, SG, JP, SG. Supervision: GR. Validation: CO, GR. Visualization: CO, GR. Writing—original draft preparation: GR, CO. Writing—review and editing: GR, CO, HD, FR, JP, VF, SG.

600 *Competing interests.* We declare no competing interests.

*Acknowledgements.* We thank A. Biggin, H. Brown, C. Davies, A. Ferreira, M. Holdt, P. Japsen, P. Koelemeijer, F. M<sup>c</sup>Nab, R. Myhill and J. Ward for helpful discussion. We also thank N. Flament and an anonymous reviewer for helping us to clarify our thesis. C.O., J.P. and V.M.F. were supported by NERC Grant NE/T01684/1.



## 605 References

- Al-Hajri, Y., White, N., and Fishwick, S.: Scales of transient convective support beneath Africa, *Geology*, 37, 883–886, <https://doi.org/10.1130/G25703A.1>, 2009.
- Bahadori, A., Holt, W., and Feng, R. e. a.: Coupled influence of tectonics, climate, and surface processes on landscape evolution in southwestern North America., *Nat Commun*, 13, <https://doi.org/10.1038/s41467-022-31903-2>, 2022.
- 610 Ball, P. W., White, N. J., Maclennan, J., and Stephenson, S. N.: Global Influence of Mantle Temperature and Plate Thickness on Intraplate Volcanism, *Nature Communications*, 12, 1–13, <https://doi.org/10.1038/s41467-021-22323-9>, 2021.
- Ball, P. W., Duvernay, T., and Davies, D. R.: A coupled geochemical-geodynamic approach for predicting mantle melting in space and time, *Geochemistry, Geophysics, Geosystems*, 23, 1–31, <https://doi.org/10.1029/2022gc010421>, 2022.
- Bangerth, W., Dannberg, J., Fraters, M., Gassmoeller, R., Glerum, A., Heister, T., Myhill, R., and Naliboff, J.: ASPECT v2.5.0, <https://doi.org/10.5281/zenodo.8200213>, 2023.
- 615 Bauer, S., Huber, M., Ghelichkhan, S., Mohr, M., Rüde, U., and Wohlmuth, B.: Large-scale simulation of mantle convection based on a new matrix-free approach, *Journal of Computational Science*, 31, 60–76, <https://doi.org/10.1016/j.joocs.2018.12.006>, 2019.
- Baumgardner, J. R.: Three-dimensional treatment of convective flow in the Earth's mantle, *Journal of Statistical Physics*, 39, 501–511, <https://doi.org/10.1007/BF01008348>, 1985.
- 620 Becker, T. W. and Boschi, L.: A comparison of tomographic and geodynamic mantle models, *Geochemistry, Geophysics, Geosystems*, 3, 1–48, <https://doi.org/10.1029/2001GC000168>, 2002.
- Biggin, A. J., Steinberger, B., Aubert, J., Suttie, N., Holme, R., Torsvik, T. H., Van Der Meer, D. G., and Van Hinsbergen, D. J.: Possible links between long-term geomagnetic variations and whole-mantle convection processes, *Nature Geoscience*, 5, 526–533, <https://doi.org/10.1038/ngeo1521>, 2012.
- 625 Braun, J.: The many surface expressions of mantle dynamics, *Nature Geoscience*, 3, 825–833, <https://doi.org/10.1038/ngeo1020>, 2010.
- Bunge, H.-P. and Baumgardner, J. R.: Mantle convection modeling on parallel virtual machines, *Computers in Physics*, 9, 207–215, <https://doi.org/10.1063/1.168525>, 1995.
- Bunge, H.-P., Richards, M. A., and Baumgardner, J. R.: Mantle-circulation models with sequential data assimilation: Inferring present-day mantle structure from plate-motion histories, *Philosophical Transactions of the Royal Society A: Mathematical, Physical and Engineering*
- 630 *Sciences*, 360, 2545–2567, <https://doi.org/10.1098/rsta.2002.1080>, 2002.
- Bunge, H.-P., Hagelberg, C. R., and Travis, B. J.: Mantle circulation models with variational data assimilation: inferring past mantle flow and structure from plate motion histories and seismic tomography, *Geophysical Journal International*, 152, 280–301, <https://doi.org/10.1046/j.1365-246X.2003.01823>, 2003.
- Cao, Z. and Liu, L.: Origin of Three-Dimensional Crustal Stress Over the Conterminous United States, *Journal of Geophysical Research: Solid Earth*, 126, e2021JB022137, <https://doi.org/https://doi.org/10.1029/2021JB022137>, e2021JB022137 2021JB022137, 2021.
- 635 Chang, C. and Liu, L.: Investigating the formation of the Cretaceous Western Interior Seaway using landscape evolution simulations, *GSA Bulletin*, 133, 347–361, <https://doi.org/10.1130/B35653.1>, 2021.
- Colli, L., Ghelichkhan, S., and Bunge, H.-P.: On the ratio of dynamic topography and gravity anomalies in a dynamic Earth, *Geophysical Research Letters*, 43, 2510–2516, <https://doi.org/10.1002/2016GL067929>, 2016.



- 640 Colli, L., Ghelichkhan, S., Bunge, H.-P., and Oeser, J.: Retrodictions of Mid Paleogene mantle flow and dynamic topography in the Atlantic region from compressible high resolution adjoint mantle convection models: Sensitivity to deep mantle viscosity and tomographic input model, *Gondwana Research*, 53, 252–272, <https://doi.org/10.1016/j.gr.2017.04.027>, 2018.
- Corrieu, V., Thoraval, C., and Ricard, Y.: Mantle dynamics and geoid Green functions, *Geophysical Journal International*, 120, 516–523, <https://doi.org/10.1111/j.1365-246X.1995.tb01835.x>, 1995.
- 645 Craig, C. H. and McKenzie, D.: Surface deformation, gravity and the geoid from a three-dimensional convection model at low Rayleigh numbers, *Earth and Planetary Science Letters*, 83, 123–136, [https://doi.org/10.1016/0012-821X\(87\)90056-2](https://doi.org/10.1016/0012-821X(87)90056-2), 1987.
- Cramer, F., Schmeling, H., Golabek, G. J., Duretz, T., Orendt, R., Buitter, S. J., May, D. A., Kaus, B. J., Gerya, T. V., and Tackley, P. J.: A comparison of numerical surface topography calculations in geodynamic modelling: An evaluation of the ‘sticky air’ method, *Geophysical Journal International*, 189, 38–54, <https://doi.org/10.1111/j.1365-246X.2012.05388.x>, 2012.
- 650 Czarnota, K., Hoggard, M. J., White, N., and Winterbourne, J.: Spatial and temporal patterns of Cenozoic dynamic topography around Australia, *Geochemistry, Geophysics, Geosystems*, 14, 634–658, <https://doi.org/10.1029/2012GC004392>, 2013.
- Dannberg, J., Eilon, Z., Faul, U., Gassmüller, R., Moulik, P., and Myhill, R.: The importance of grain size to mantle dynamics and seismological observations, *Geochemistry, Geophysics, Geosystems*, 18, 3034–3061, <https://doi.org/10.1002/2017GC006944>, 2017.
- Davies, D. R., Davies, J. H., Bollada, P. C., Hassan, O., Morgan, K., and Nithiarasu, P.: A hierarchical mesh refinement technique for global 3-D spherical mantle convection modelling, *Geoscientific Model Development*, 6, 1095–1107, <https://doi.org/10.5194/gmd-6-1095-2013>, 2013.
- 655 Davies, D. R., Valentine, A. P., Kramer, S. C., Rawlinson, N., Hoggard, M. J., Eakin, C. M., and Wilson, C. R.: Earth’s multi-scale topographic response to global mantle flow, *Nature Geoscience*, 12, 845–850, <https://doi.org/10.1038/s41561-019-0441-4>, 2019.
- Davies, D. R., Ghelichkhan, S., Hoggard, M. J., Valentine, A. P., and Richards, F. D.: Observations and Models of Dynamic Topography: Current Status and Future Directions, in: *Dynamics of Plate Tectonics and Mantle Convection*, edited by Duarte, J., chap. 11, pp. 223–269, Elsevier, <https://doi.org/10.1016/B978-0-323-85733-8.00017-2>, 2023.
- 660 Fernandes, V. M. and Roberts, G. G.: Cretaceous to Recent net continental uplift from paleobiological data: Insights into sub-plate support, *GSA Bulletin*, 133, 1–20, <https://doi.org/10.1130/b35739.1>, 2021.
- Fernandes, V. M., Roberts, G. G., White, N., and Whittaker, A. C.: Continental-Scale Landscape Evolution: A History of North American Topography, *Journal of Geophysical Research: Earth Surface*, 124, 1–34, <https://doi.org/10.1029/2018jf004979>, 2019.
- 665 Fichtner, A. and Villaseñor, A.: Crust and upper mantle of the western Mediterranean - Constraints from full-waveform inversion, *Earth and Planetary Science Letters*, 428, 52–62, <https://doi.org/10.1016/j.epsl.2015.07.038>, 2015.
- Fichtner, A., Kennett, B. L. N., Igel, H., and Bunge, H.-P.: Full seismic waveform tomography for upper-mantle structure in the Australasian region using adjoint methods, *Geophysical Journal International*, 179, 1703–1725, <https://doi.org/10.1111/j.1365-246X.2009.04368.x>, 2009.
- 670 Fichtner, A., Trampert, J., Cupillard, P., Saygin, E., Taymaz, T., Capdeville, Y., and Villaseñor, A.: Multiscale full waveform inversion, *Geophysical Journal International*, 194, 534–556, <https://doi.org/10.1093/gji/ggt118>, 2013.
- Flament, N.: Present-day dynamic topography and lower-mantle structure from palaeogeographically constrained mantle flow models, *Geophysical Journal International*, 216, 2158–2182, <https://doi.org/10.1093/gji/ggy526>, 2019.
- 675 Flament, N., Gurnis, M., and Muller, R. D.: A review of observations and models of dynamic topography, *Lithosphere*, 5, 189–210, <https://doi.org/10.1130/L245.1>, 2013.



- Flament, N., Gurnis, M., Williams, S., Seton, M., Skogseid, J., Heine, C., and Dietmar Müller, R.: Topographic asymmetry of the South Atlantic from global models of mantle flow and lithospheric stretching, *Earth and Planetary Science Letters*, 387, 107–119, <https://doi.org/10.1016/j.epsl.2013.11.017>, 2014.
- 680 Flament, N., Gurnis, M., Müller, R. D., Bower, D. J., and Husson, L.: Influence of subduction history on South American topography, *Earth and Planetary Science Letters*, 430, 9–18, <https://doi.org/10.1016/j.epsl.2015.08.006>, 2015.
- Foley, S. F. and Fischer, T. P.: An essential role for continental rifts and lithosphere in the deep carbon cycle, *Nature Geoscience*, 10, 897–902, <https://doi.org/10.1038/s41561-017-0002-7>, 2017.
- Forte, A. M.: Constraints on Seismic Models from Other Disciplines - Implications for Mantle Dynamics and Composition, in: *Seismology and the Structure of the Earth*, edited by Romanowicz, B. and Dziewonski, A., chap. 1.23, pp. 805–858, Elsevier B.V., ISBN 9780444527486, <https://doi.org/10.1016/B978-044452748-6.00027-4>, 2007.
- 685 Forte, A. M. and Peltier, R.: Viscous Flow Models of Global Geophysical Observables 1. Forward Problems, *Journal of Geophysical Research*, 96, 20 131–20 159, <https://doi.org/10.1029/91JB01709>, 1991.
- Forte, A. M. and Peltier, W. R.: The Kinematics and Dynamics of Poloidal-Toroidal Coupling in Mantle Flow: The Importance of Surface  
690 Plates and Lateral Viscosity Variations, *Advances in Geophysics*, 36, 1–119, [https://doi.org/10.1016/S0065-2687\(08\)60537-3](https://doi.org/10.1016/S0065-2687(08)60537-3), 1994.
- French, S. W. and Romanowicz, B.: Broad plumes rooted at the base of the Earth’s mantle beneath major hotspots, *Nature*, 525, 95–99, <https://doi.org/10.1038/nature14876>, 2015.
- Galloway, W. E., Whiteaker, T. L., and Ganey-Curry, P.: History of Cenozoic North American drainage basin evolution, sediment yield, and accumulation in the Gulf of Mexico basin, *Geosphere*, 7, 938–973, <https://doi.org/10.1130/GES00647.1>, 2011.
- 695 Gantmacher, F. R.: *The Theory of Matrices*, Chelsea Publishing Company, New York, 1959.
- Ghelichkhan, S., Bunge, H.-P., and Oeser, J.: Global mantle flow retrodictions for the early Cenozoic using an adjoint method: Evolving dynamic topographies, deep mantle structures, flow trajectories and sublithospheric stresses, *Geophysical Journal International*, 226, 1432–1460, <https://doi.org/10.1093/gji/ggab108>, 2021.
- Ghosh, A. and Holt, W. E.: Plate Motions and Stresses from Global Dynamic Models, *Science*, 335, 838–843, <https://doi.org/10.1126/science.1214209>, 2012.
- 700 Ghosh, A., Becker, T. W., and Zhong, S. J.: Effects of lateral viscosity variations on the geoid, *Geophysical Research Letters*, 37, 2–7, <https://doi.org/10.1029/2009GL040426>, 2010.
- Glišović, P. and Forte, A. M.: A new back-and-forth iterative method for time-reversed convection modeling: Implications for the Cenozoic evolution of 3-D structure and dynamics of the mantle, *Journal of Geophysical Research: Solid Earth*, 121, 4067–4084, <https://doi.org/10.1002/2016JB012841>, 2016.
- 705 Gunnell, Y. and Burke, K.: The African Erosion Surface: A Continental-Scale Synthesis of Geomorphology, Tectonics, and Environmental Change over the Past 180 Million Years, *Memoir of the Geological Society of America*, 201, 1–66, <https://doi.org/10.1130/2008.1201.2008>.
- Gurnis, M., Mitrovica, J. X., Ritsema, J., and Van Heijst, H.-J.: Constraining mantle density structure using geological evidence of surface uplift rates: The case of the African Superplume, *Geochemistry, Geophysics, Geosystems*, 1, 1–35, <https://doi.org/10.1029/1999GC000035>, 2000.
- 710 Hager, B. H.: Subducted Slabs and the Geoid: Constraints on Mantle Rheology and Flow, *Journal of Geophysical Research*, 89, 6003–6015, 1984.





- Hager, B. H. and Clayton, R. W.: Constraints on the Structure of Mantle Convection Using Seismic Observations, Flow Models, and the Geoid, in: *Mantle Convection: Plate Tectonics and Global Dynamics*, edited by Peltier, W. R., chap. 9, pp. 657–763, Gordon and Breach Science Publishers, New York, 1989.
- Hager, B. H. and O’Connell, R. J.: Kinematic Models of Large-Scale Flow in the Earth’s Mantle, *Journal of Geophysical Research*, 84, 1031–1048, 1979.
- Hager, B. H. and O’Connell, R. J.: A Simple Global Model of Plate Dynamics and Mantle Convection, *Journal of Geophysical Research*, 86, 4843–4867, <https://doi.org/10.1029/JB086iB06p04843>, 1981.
- Hager, B. H., Clayton, R. W., Richards, M. A., Comer, R. P., and Dziewonski, A. M.: Lower mantle heterogeneity, dynamic topography and the geoid, *Nature*, 313, 541–545, <https://doi.org/10.1038/314752a0>, 1985.
- Hazzard, J. A. N., Richards, F. D., Goes, S. D. B., and Roberts, G. G.: Probabilistic Assessment of Antarctic Thermomechanical Structure: Impacts on Ice Sheet Stability, *EarthArXiv*, <https://doi.org/10.31223/X5C35R>, 2022.
- Heister, T., Dannberg, J., Gassmüller, R., and Bangerth, W.: High accuracy mantle convection simulation through modern numerical methods – II: realistic models and problems, *Geophysical Journal International*, 210, 833–851, <https://doi.org/10.1093/gji/ggx195>, 2017.
- Hoggard, M. J., White, N., and Al-Attar, D.: Global dynamic topography observations reveal limited influence of large-scale mantle flow, *Nature Geoscience*, 9, 1–8, <https://doi.org/10.1038/ngeo2709>, 2016.
- Hoggard, M. J., Austermann, J., Randel, C., and Stephenson, S.: Observational Estimates of Dynamic Topography Through Space and Time, in: *Mantle Convection and Surface Expressions*, July, chap. 15, pp. 371–411, AGU, ISBN 9781119528609, <https://doi.org/10.1002/9781119528609.ch15>, 2021.
- Holdt, M. C., White, N. J., Stephenson, S. N., and Conway-Jones, B. W.: Densely Sampled Global Dynamic Topographic Observations and Their Significance, *Journal of Geophysical Research: Solid Earth*, 127, 1–32, 2022.
- J Jeans, J. H.: The Propagation of Earthquake Waves, *Proceedings of the Royal Society of London A*, 102, 554–574, 1923.
- Kaula, W. M.: Determination of the Earth’s Gravitational Field, *Reviews of Geophysics*, 1, 507–551, 1963.
- Kramer, S. C., Davies, D. R., and Wilson, C. R.: Analytical solutions for mantle flow in cylindrical and spherical shells, *Geoscientific Model Development*, 14, 1899–1919, <https://doi.org/10.5194/gmd-14-1899-2021>, 2021.
- Lambeck, K., Smither, C., and Johnston, P.: Sea-level change, glacial rebound and mantle viscosity for northern Europe, *Geophysical Journal International*, 134, 102–144, <https://doi.org/10.1046/j.1365-246X.1998.00541.x>, 1998.
- Lau, H. C. P., Mitrovica, J. X., Davis, J. L., Tromp, J., Yang, H.-Y., and Al-Attar, D.: Tidal tomography constrains Earth’s deep-mantle buoyancy, *Nature*, 551, 321–326, <https://doi.org/10.1038/nature24452>, 2017.
- Lees, M. E., Rudge, J. F., and McKenzie, D.: Gravity, topography, and melt generation rates from simple 3D models of mantle convection, *Geochemistry, Geophysics, Geosystems*, 21, 1–29, <https://doi.org/10.1029/2019gc008809>, 2020.
- Lekić, V. and Fischer, K. M.: Contrasting lithospheric signatures across the western United States revealed by Sp receiver functions, *Earth and Planetary Science Letters*, 402, 90–98, <https://doi.org/10.1016/j.epsl.2013.11.026>, 2014.
- Liu, L. and Gurnis, M.: Simultaneous inversion of mantle properties and initial conditions using an adjoint of mantle convection, *Journal of Geophysical Research: Solid Earth*, 113, 1–17, <https://doi.org/10.1029/2008jb005594>, 2008.
- Liu, S. and King, S. D.: A benchmark study of incompressible Stokes flow in a 3-D spherical shell using ASPECT, *Geophysical Journal International*, 217, 650–667, <https://doi.org/10.1093/gji/ggz036>, 2019.



- 750 Lu, C., Forte, A. M., Simmons, N. A., Grand, S. P., Kajan, M. N., Lai, H., and Garnero, E. J.: The Sensitivity of Joint Inversions of Seismic and Geodynamic Data to Mantle Viscosity, *Geochemistry, Geophysics, Geosystems*, 21, 1–29, <https://doi.org/10.1029/2019gc008648>, 2020.
- McKenzie, D.: Surface deformation, gravity anomalies and convection, *Geophysical Journal of the Royal Astronomical Society*, 48, 211–238, <https://doi.org/10.1111/j.1365-246X.1977.tb01297.x>, 1977.
- 755 Merdith, A. S., Williams, S. E., Collins, A. S., Tetley, M. G., Mulder, J. A., Blades, M. L., Young, A., Armistead, S. E., Cannon, J., Zahirovic, S., and Müller, R. D.: Extending full-plate tectonic models into deep time: Linking the Neoproterozoic and the Phanerozoic, *Earth-Science Reviews*, 214, 1–44, <https://doi.org/10.1016/j.earscirev.2020.103477>, 2021.
- Mitrovica, J. X. and Forte, A. M.: A new inference of mantle viscosity based upon joint inversion of convection and glacial isostatic adjustment data, *Earth and Planetary Science Letters*, 225, 177–189, <https://doi.org/10.1016/j.epsl.2004.06.005>, 2004.
- 760 Molnar, P., England, P. C., and Jones, C. H.: Mantle dynamics, isostasy, and the support of high terrain, *Journal of Geophysical Research: Solid Earth*, 120, 1932–1957, <https://doi.org/10.1002/2014JB011724>, 2015.
- Morris, M., Fernandes, V. M., and Roberts, G. G.: Extricate dynamic topography from subsidence patterns: Examples from Eastern North America’s passive margin, *Earth and Planetary Science Letters*, 530, 1–13, <https://doi.org/10.1016/j.epsl.2019.115840>, 2020.
- Moucha, R. and Forte, A. M.: Changes in African topography driven by mantle convection: supplementary information, *Nature Geoscience*, 765 4, 707–712, <https://doi.org/10.1038/ngeo1235>, 2011.
- Moucha, R., Forte, A. M., Mitrovica, J. X., and Daradich, A.: Lateral variations in mantle rheology: Implications for convection related surface observables and inferred viscosity models, *Geophysical Journal International*, 169, 113–135, <https://doi.org/10.1111/j.1365-246X.2006.03225.x>, 2007.
- Moucha, R., Forte, A. M., Mitrovica, J. X., Rowley, D. B., Quéré, S., Simmons, N. A., and Grand, S. P.: Dynamic topography and long-term sea-level variations: There is no such thing as a stable continental platform, *Earth and Planetary Science Letters*, 271, 101–108, <https://doi.org/10.1016/j.epsl.2008.03.056>, 2008.
- 770 O’Connell, R. J.: Pleistocene Glaciation and the Viscosity of the Lower Mantle, *Geophysical Journal of the Royal Astronomical Society*, 23, 299–327, <https://doi.org/10.1111/j.1365-246X.1971.tb01823.x>, 1971.
- O’Malley, C. P. B., White, N. J., Stephenson, S. N., and Roberts, G. G.: Large-Scale Tectonic Forcing of the African Landscape, *Journal of Geophysical Research: Earth Surface*, 126, 1–37, <https://doi.org/10.1029/2021jf006345>, 2021.
- 775 Panasyuk, S. V., Hager, B. H., and Forte, A. M.: Understanding the effects of mantle compressibility on geoid kernels, *Geophysical Journal International*, 124, 121–133, <https://doi.org/10.1111/j.1365-246X.1996.tb06357.x>, 1996.
- Panton, J., Davies, J. H., and Myhill, R.: The Stability of Dense Oceanic Crust Near the Core-Mantle Boundary, *Journal of Geophysical Research: Solid Earth*, 128, 1–21, <https://doi.org/10.1029/2022JB025610>, 2023.
- 780 Parsons, B. and Daly, S.: The relationship between surface topography, gravity anomalies and temperature structure of convection, *Journal of Geophysical Research*, 88, 1129–1144, <https://doi.org/10.1029/JB088iB02p01129>, 1983.
- Pekeris, C. L.: Thermal Convection in the Interior of the Earth, *Geophysical Supplements to the Monthly Notices of the Royal Astronomical Society*, 3, 343–367, 1935.
- Priestley, K. and McKenzie, D.: The relationship between shear wave velocity, temperature, attenuation and viscosity in the shallow part of the mantle, *Earth and Planetary Science Letters*, 381, 78–91, <https://doi.org/10.1016/j.epsl.2013.08.022>, 2013.
- 785 Ribe, N. M.: Analytical Approaches to Mantle Dynamics, *Treatise on Geophysics*, 7, 167–226, <https://doi.org/10.1016/B978-044452748-6.00117-6>, 2007.



- Ricard, Y.: Physics of Mantle Convection, *Treatise on Geophysics*, 7, 31–88, 2007.
- Ricard, Y.: Physics of Mantle Convection, in: *Treatise on Geophysics*, edited by Schubert, G., chap. 7.02, pp. 23–71,  
790 <https://doi.org/10.1016/B978-044452748-6.00115-2>, 2015.
- Richards, F. D., Hoggard, M. J., White, N., and Ghelichkhan, S.: Quantifying the relationship between short-wavelength dynamic topography and thermomechanical structure of the upper mantle using calibrated parameterization of anelasticity, *Journal of Geophysical Research: Solid Earth*, 125, 1–36, <https://doi.org/10.1029/2019JB019062>, 2020.
- Richards, F. D., Hoggard, M. J., Ghelichkhan, S., Koelemeijer, P., and Lau, H. C. P.: Geodynamic, geodetic, and seismic constraints favour  
795 deflated and dense-cored LLVPs, *Earth and Planetary Science Letters*, 602, 1–13, <https://doi.org/10.1016/j.epsl.2022.117964>, 2023.
- Richards, M. A. and Hager, B. H.: Geoid Anomalies in a Dynamic Earth, *Journal of Geophysical Research*, 89, 5987–6002, <https://doi.org/10.1029/JB089iB07p05987>, 1984.
- Salles, T., Flament, N., and Müller, D.: Influence of mantle flow on the drainage of eastern Australia since the Jurassic Period, *Geochemistry, Geophysics, Geosystems*, 18, 280–305, <https://doi.org/10.1002/2016GC006617>, 2017.
- 800 Spasojevic, S. and Gurnis, M.: Sea level and vertical motion of continents from dynamic earth models since the Late Cretaceous, *AAPG Bulletin*, 96, 2037–2064, <https://doi.org/10.1306/03261211121>, 2012.
- Stanley, J. R., Braun, J., Baby, G., Guillocheau, F., Robin, C., Flowers, R. M., Brown, R., Wildman, M., and Beucher, R.: Constraining Plateau Uplift in Southern Africa by Combining Thermochronology, Sediment Flux, Topography, and Landscape Evolution Modeling, *Journal of Geophysical Research: Solid Earth*, 126, 1–34, <https://doi.org/10.1029/2020JB021243>, 2021.
- 805 Steinberger, B.: Effects of latent heat release at phase boundaries on flow in the Earth’s mantle, phase boundary topography and dynamic topography at the Earth’s surface, *Physics of the Earth and Planetary Interiors*, 164, 2–20, <https://doi.org/10.1016/j.pepi.2007.04.021>, 2007.
- Steinberger, B.: Topography caused by mantle density variations: Observation-based estimates and models derived from tomography and lithosphere thickness, *Geophysical Journal International*, 205, 604–621, <https://doi.org/10.1093/gji/ggw040>, 2016.
- 810 Steinberger, B. and Antretter, M.: Conduit diameter and buoyant rising speed of mantle plumes: Implications for the motion of hot spots and shape of plume conduits, *Geochemistry, Geophysics, Geosystems*, 7, 1–25, <https://doi.org/10.1029/2006GC001409>, 2006.
- Steinberger, B. and Calderwood, A. R.: Models of large-scale viscous flow in the Earth’s mantle with constraints from mineral physics and surface observations, *Geophysical Journal International*, 167, 1461–1481, <https://doi.org/10.1111/j.1365-246X.2006.03131.x>, 2006.
- Steinberger, B., Nelson, P. L., Grand, S. P., and Wang, W.: Yellowstone plume conduit tilt caused by large-scale mantle flow, *Geochemistry, Geophysics, Geosystems*, 20, 5896–5912, <https://doi.org/10.1029/2019gc008490>, 2019.
- 815 Stephenson, S. N., White, N. J., Carter, A., Seward, D., Ball, P. W., and Klöcking, M.: Cenozoic Dynamic Topography of Madagascar, *Geochemistry, Geophysics, Geosystems*, 22, 1–38, <https://doi.org/10.1029/2020gc009624>, 2021.
- Tackley, P. J., Stevenson, D. J., Glatzmaier, G. A., and Schubert, G.: Effects of an endothermic phase transition at 670 km depth on spherical mantle convection, *Nature*, 361, 699–704, <https://doi.org/10.1038/361699a0>, 1993.
- 820 Thoraval, C. and Richards, M. A.: The geoid constraint in global geodynamics: Viscosity structure, mantle heterogeneity models and boundary conditions, *Geophysical Journal International*, 131, 1–8, <https://doi.org/10.1111/j.1365-246X.1997.tb00591.x>, 1997.
- Thoraval, C., Machete, P., and Cazenave, A.: Influence of mantle compressibility and ocean warping on dynamical models of the geoid, *Geophysical Journal International*, 117, 566–573, <https://doi.org/10.1111/j.1365-246X.1994.tb03954.x>, 1994.
- Turcotte, D. L. and Schubert, G.: *Geodynamics*, Cambridge University Press, second edi edn., ISBN 0521661862, 2002.



- 825 Wang, Y., Liu, L., and Zhou, Q.: Topography and Gravity Reveal Denser Cratonic Lithospheric Mantle Than Previously Thought, *Geophysical Research Letters*, 49, <https://doi.org/10.1029/2021GL096844>, 2022.
- Wieczorek, M. A. and Meschede, M.: SHTools: Tools for Working with Spherical Harmonics, *Geochemistry, Geophysics, Geosystems*, 19, 1–19, <https://doi.org/10.1029/2018GC007529>, 2018.
- Zhong, S., Gurnis, M., and Hulbert, G.: Accurate determination of surface normal stress in viscous flow from a consistent boundary flux method, *Physics of the Earth and Planetary Interiors*, 78, 1–8, [https://doi.org/10.1016/0031-9201\(93\)90078-N](https://doi.org/10.1016/0031-9201(93)90078-N), 1993.
- 830 Zhong, S., Zuber, M. T., Moresi, L., and Gurnis, M.: Role of temperature-dependent viscosity and surface plates in spherical shell models of mantle convection, *Journal of Geophysical Research*, 105, 11 063–11 082, 2000.
- Zhong, S., McNamara, A., Tan, E., Moresi, L., and Gurnis, M.: A benchmark study on mantle convection in a 3-D spherical shell using CitcomS, *Geochemistry, Geophysics, Geosystems*, 9, 1–32, <https://doi.org/10.1029/2008GC002048>, 2008.
- 835 Zhou, Q. and Liu, L.: Topographic evolution of the western United States since the early Miocene, *Earth and Planetary Science Letters*, 514, 1–12, <https://doi.org/10.1016/j.epsl.2019.02.029>, 2019.
- Zhou, Q., Liu, L., and Hu, J.: Western US volcanism due to intruding oceanic mantle driven by ancient Farallon slabs, *Nature Geoscience*, 11, 70–76, <https://doi.org/10.1038/s41561-017-0035-y>, 2018.

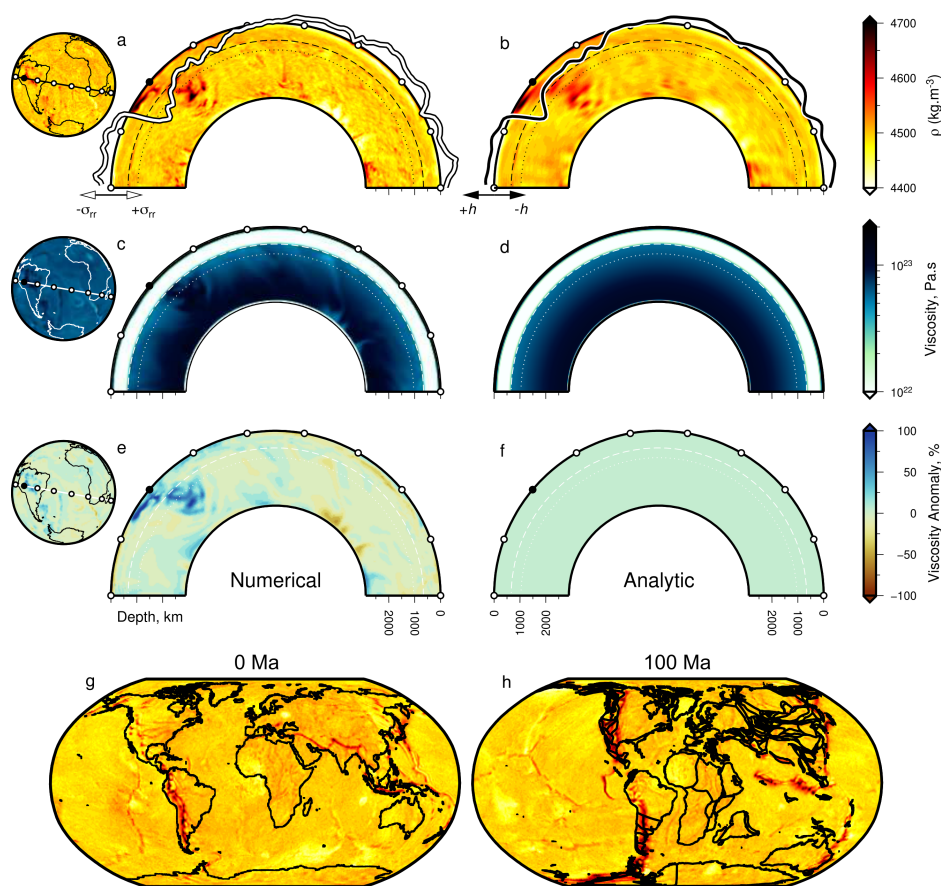


**Figure 1. Examples of mantle densities and viscosity used to calculate stresses and surface deflections numerically and analytically.**

(a) Great-circle slice (180°) through full-resolution, present-day, density  $\rho$ , predicted by numeric model TERRA with temperature dependent viscosity (Model 11a; see Table 1 and body text); see globe to left for location. White circles = 20° intervals; filled black circle indicates orientation of cross section; dashed line = 660 km depth contour; dotted line = 1038 km depth contour, at which depth  $\rho$  is plotted on globe; white-black curve = numeric prediction of surface normal stress  $\sigma_{rr}$  from Model 11a. (b) As (a) but slice is through spherical harmonic expansion of density structure, to maximum degree  $l = 50$  ( $\lambda \approx 792$  km; Model 11b); black-white curve = surface deflection  $h$ , calculated using (analytic) propagator matrix approach (Model 12). (c) As (a) but for slice through full-resolution viscosity structure of numeric model. (d) As (c) but for mean (radial) viscosity structure, used along with the density structure shown in (b) to generate analytic solution for surface deflection shown by black-white curve atop (b). (e–f) As (c–d) but viscosity is expressed as a percentage anomaly with respect to the layer (radial) mean. (g–h) Predicted densities at 270 km depth at 0 and 100 Ma from numeric model with viscosity independent of temperature (Model 1a). Extended results are shown in Figure S1. Plate motions and paleo-coastlines are from Merdith2021.

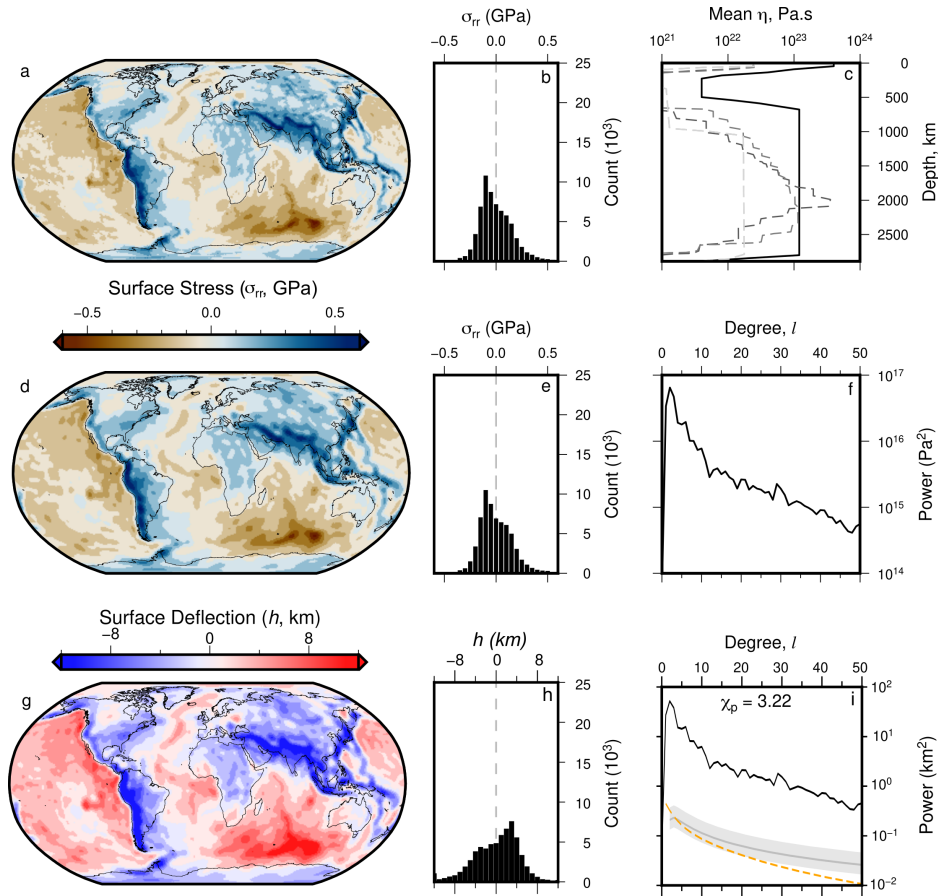


**Figure 2. Surface stresses and deflections from numeric simulation of mantle convection with spherical harmonic expansion up to degree 50.** (a) Predicted present-day surface radial stress,  $\sigma_{rr}$  (Model 1a). (b) Histogram of values shown in (a). (c) Black line = radial viscosity structure used to drive Model 1a and thus produce grid shown in panel (a). Gray dashed lines = alternative viscosity profiles of (from darkest to lightest) Mitrovica2004, Steinberger2006a, and  $\mu_1$ ,  $\mu_2$  from Ghelichkhan2021. (d) Model 1b: Spherical harmonic fit to Model 1a (panel a) up to maximum degree  $l = 50$  (minimum wavelength  $\lambda \approx 792$  km). (e) Histogram of values shown in panel (d). (f) Power spectrum—total power per degree—of stress field shown in panel (d). (g) Spherical harmonic fit to surface deflections (Model 1b; up to degree  $l = 50$ ). (h) Histogram of values shown in panel (g). (i) Black curve = power spectrum of calculated water-loaded surface deflections (panel g); gray line and band = expected dynamic topography from Kaula’s rule using admittance  $Z = 12 \pm 3$  mGal km<sup>-1</sup> (Kaula, 1963). Orange dashed line = expected power spectrum for water-loaded residual topography (from Holdt et al., 2022) via analytic solution of special case of Equation 15.  $\chi_p$  = root-mean-squared difference between calculated (black) and independent (orange & grey) surface deflection power (see Equation 20). All histograms are weighted by latitude to correct to equal-area. Figure S2 shows extended results including air-loaded deflections.



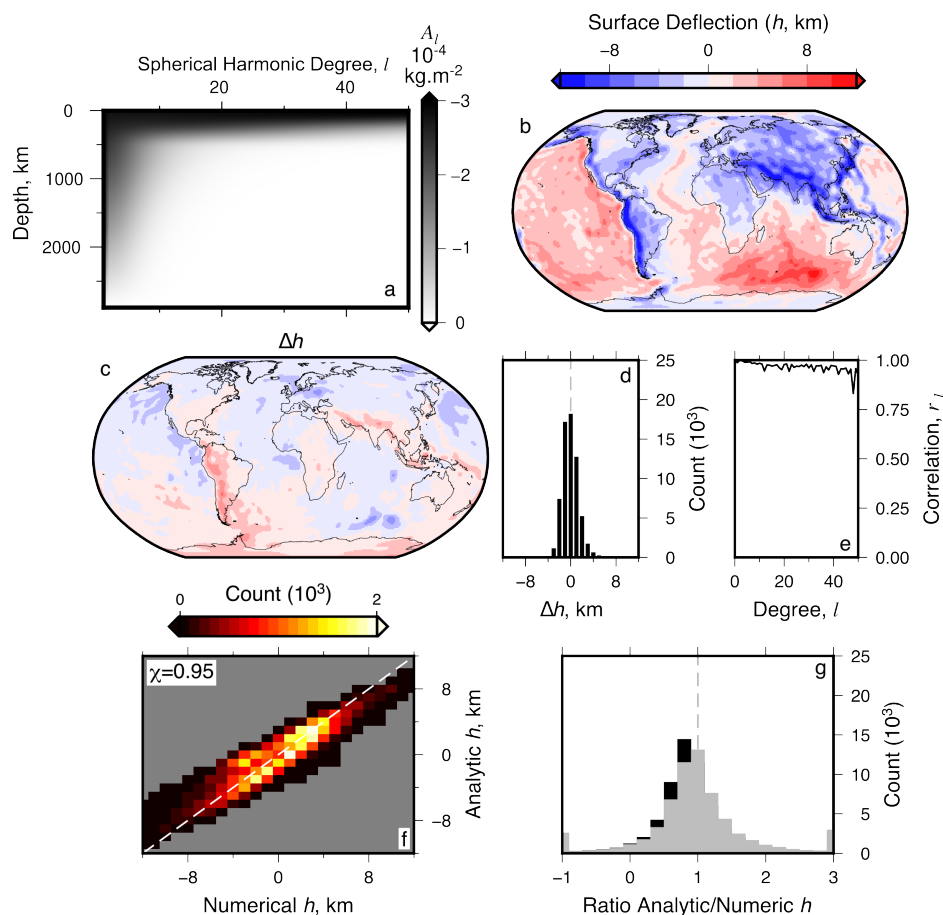


**Figure 3. Comparisons of numeric (Model 1b) and analytic (Model 2) estimation of surface deflections from models with identical parameterization.** (a) Surface deflection sensitivity kernel  $A_l$  as a function of spherical harmonic degree,  $l$ , and depth (Model 2). (b) Propagator matrix (analytic) solution for water-loaded surface deflection calculated using sensitivity kernel shown in panel (a). Figure S3 shows extended results including power spectra and air-loaded deflections. (c) Difference,  $\Delta h$ , of surface deflections in Models 1b and 2. (d) Histogram of difference values shown in (c). (e) Spectral correlation coefficient,  $r_l$ , between Models 1b and 2; Equation 8. (f) Comparison of predicted surface deflections;  $\chi$  = root-mean-squared difference between predictions (Equation 7); gray dashed line = 1:1 ratio. (g) Black bars = histogram of ratios between analytic:numeric solutions for surface deflection as in (f). Gray dashed line = 1 (i.e., identical values). Gray bars = as black bars, but for propagator matrix solution amplitudes scaled up by optimal factor to fit numeric solution (=10%). All histograms are weighted by latitude to correct to equal-area.



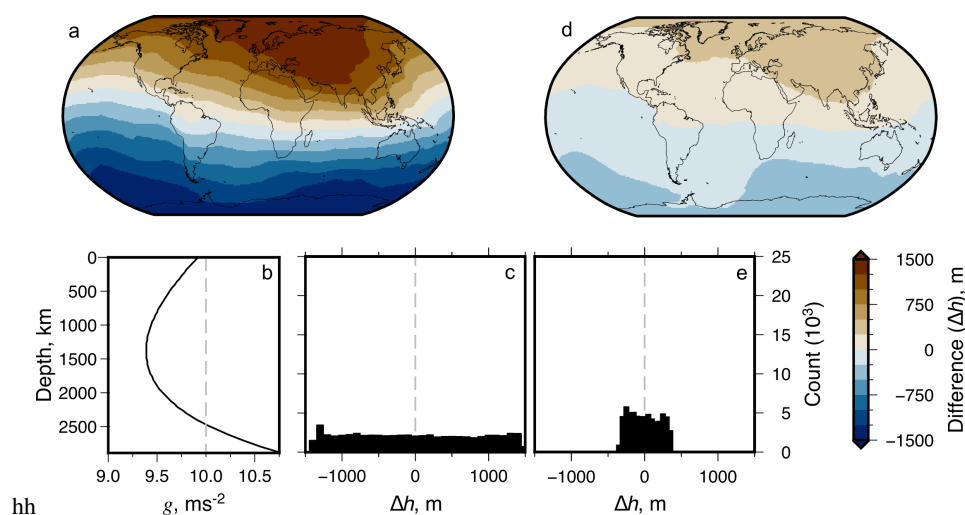


**Figure 4. Impact of self-gravitation (a–c) and gravitational potential of deflected surfaces (d–e) on surface deflections calculated analytically.** In these tests surface deflections from models with different gravity parameterizations are compared to predictions from Model 2. (a) Difference between water-loaded surface deflections calculated using the propagator matrix technique incorporating self-gravitation (Model 3; black curve in panel b) and  $g = 10 \text{ m s}^{-2}$  (dashed line in panel b; Model 2). (c) Histogram of values in panel (a). (d–e) Differences in surface deflection from models with (Model 4) and without (Model 2) stress perturbations induced by gravitational potential of the deflected surface. All histograms are weighted by latitude to correct to equal-area, they show the full extent of the results. Figures S4–S5 show extended results including maps of calculated surface deflections.

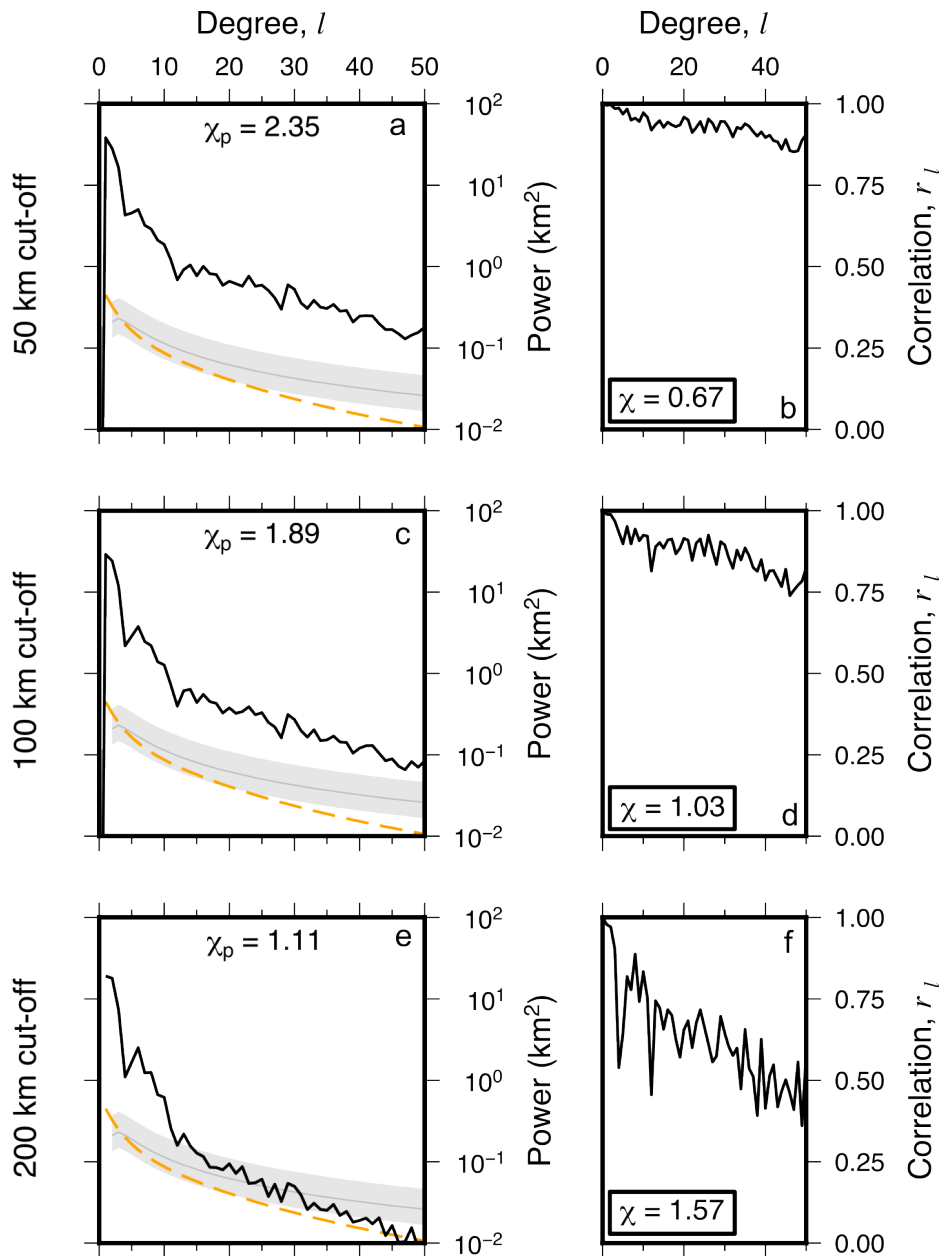


**Figure 5. Effect of removing shallow structure on surface deflections calculated analytically.** Surface deflections in models with shallow structure removed are compared to those predicted by Model 2. (a) Black line = Power spectra of predicted water-loaded surface deflection from propagator matrix solution for Model 2 (Figure 3b), but with effect of upper 50 km of density anomaly structure ignored in calculation (Model 5). Gray line and band = expected dynamic topography from Kaula's rule using admittance  $Z = 12 \pm 3 \text{ mGal km}^{-1}$  (Kaula, 1963). Orange dashed line = expected power spectrum for water-loaded residual topography from Holdt et al. (2022), via analytic solution of special case of Equation 15.  $\chi_p$  = root-mean-squared difference between calculated (black) and independent (orange & grey) surface deflection power (see Equation 20). (b) Spectral correlation coefficient,  $r_l$ , of surface deflections in Models 5 and 2 (see Equation 19). Inset  $\chi$  = root-mean-squared difference in surface deflections of Models 5 and 2 (see Equation 18). (c–d) and (e–f) as (a–b) but for depth cut-offs of 100 (Model 6) and 200 km (Model 7), respectively. Figure S7 shows extended results including maps of calculated surface deflections and differences with Model 2.

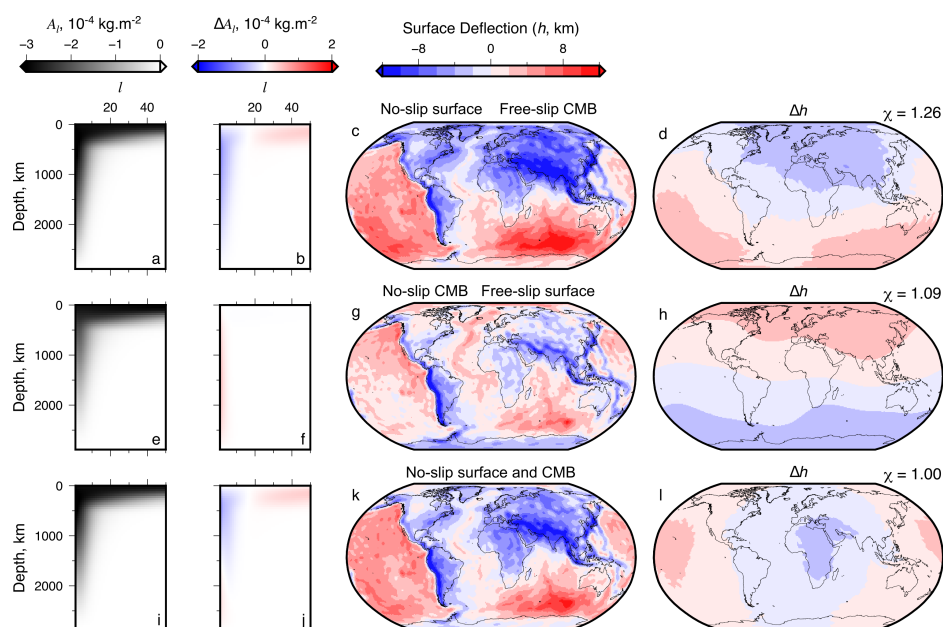


**Figure 6. Impact of free- and no-slip surface and core-mantle boundary boundary conditions on surface deflections.** This figure shows comparisons of surface deflections from models with different assumed boundary conditions and Model 2. (a) Water-loaded surface deflection sensitivity kernel  $A_l$ , for Model 8, which has a no-slip surface boundary condition, but otherwise is parameterised the same as Model 2. (b) Sensitivity kernel of Model 8 minus sensitivity kernel of Model 2. Note, positive difference implies reduced sensitivity compared to Model 2, and vice versa, since  $A_l$  is negative. (c) Predicted water-loaded surface deflection for Model 8. (d) Difference between surface deflection predictions for Model 8 and Model 2. (e–h) as (a–d) but for Model 9: free-slip surface boundary, no-slip CMB. (i–l) as (a–d) but for Model 10: no-slip surface and CMB boundaries.

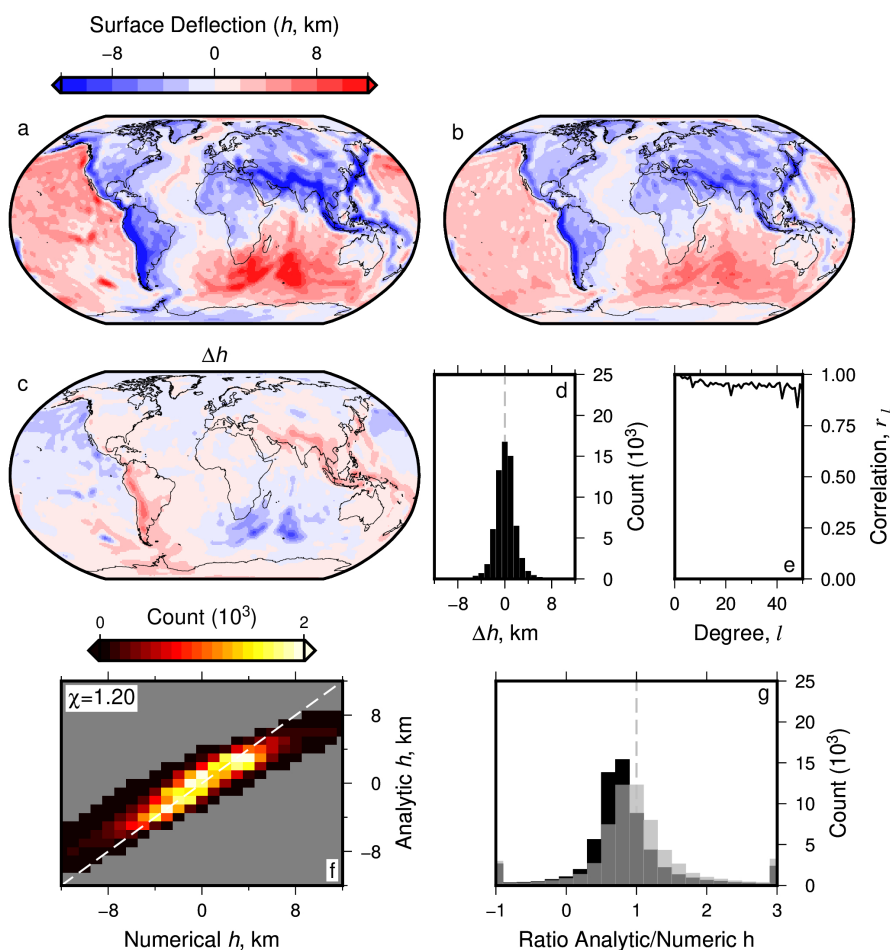


**Figure 7. Comparison of surface deflections calculated numerically (Model 11b) and analytically (Model 12) using results from simulation with temperature dependent viscosity.** (a) Model 11b: Spherical harmonic expansion of predicted present-day water-loaded surface deflection converted from stress output from numeric model TERRA (Model 11a), to maximum degree  $l = 50$ . (b) Model 12: As (a) but for prediction made using propagator matrix method. (c) Difference,  $\Delta h$ , between Models 11b and 12 (panels a and b). (d) Histogram of difference values shown in (c), weighted by latitude to correct to equal-area. (e) Spectral correlation coefficient,  $r_l$ , between predictions shown in panels (a) and (b); Equation 8. (f) Numeric (Model 11b) versus analytic (Model 12) predictions of surface deflection;  $\chi$  = root-mean-squared difference between predictions, Equation 7; gray dashed line = 1:1 ratio. (g) Histogram of ratios between analytic:numeric solutions for surface deflection as in (f), weighted by latitude. Gray dashed line = 1 (i.e., identical values). Gray bars = as black bars, but for propagator matrix solution amplitudes scaled up by optimal factor to fit numeric solution (24%).

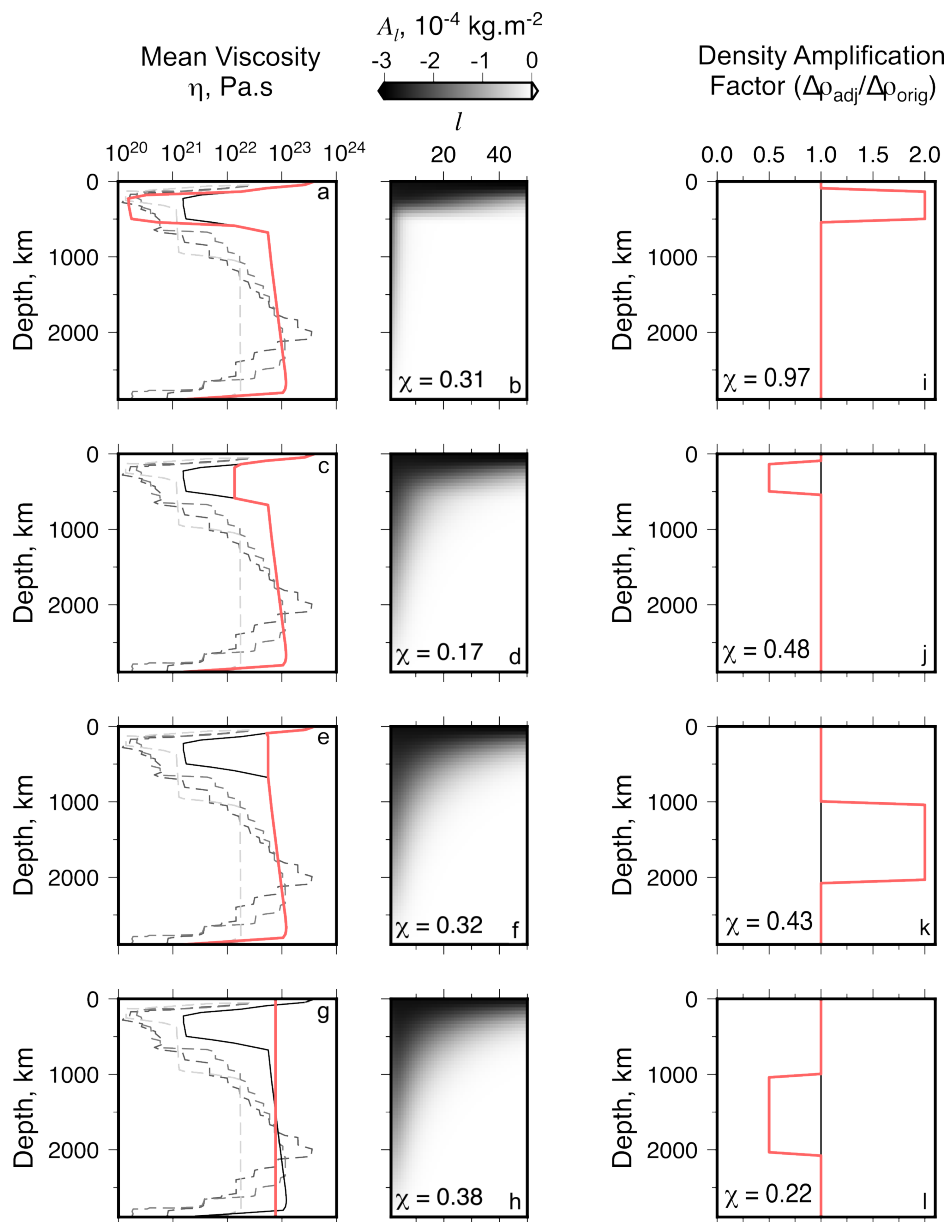




**Figure 8. Sensitivity of calculated analytic surface deflection to adjusted radial viscosity (a–h) and density anomalies (i–l).** This figure shows comparisons of surface deflections calculated in models with modified viscosity and density to the results from Model 12 (see Table 1). (a) Black curve = unadjusted prediction of present-day radial mean viscosity from Model 11; red line = adjusted radial profile with viscosity decreased by a factor of 10 between depths of  $\sim 300$ – $500$  km (Model 13); gray dashed lines = viscosity profiles used in other studies (see Figure 2). (b) Sensitivity kernel for the viscosity profile indicated by the red curve in panel a. Value of root-mean-squared difference,  $\chi$ , between calculated surface deflections for unadjusted and adjusted viscosity is stated (see Equation 7). (c–h) Results from testing alternative radial viscosity (Models 14–16). Figure S13 shows extended results including maps of surface deflections and their differences. (i–l) Density anomalies (red line) adjusted by directly scaling spherical harmonic coefficients ( $l > 0$ ) up or down by a factor of 2 (Models 17 & 19: panels e & g) or  $\frac{1}{2}$  (Models 18 & 20: f & h). Viscosity structure applied in each case is same as that used to generate Figure 7b. Sensitivity kernels for surface deflections are not shown since they are invariant with respect to density anomalies,  $\Delta\rho$ , depending only on viscosity structure. Figure S14 shows extended results including maps of surface deflections and their differences.

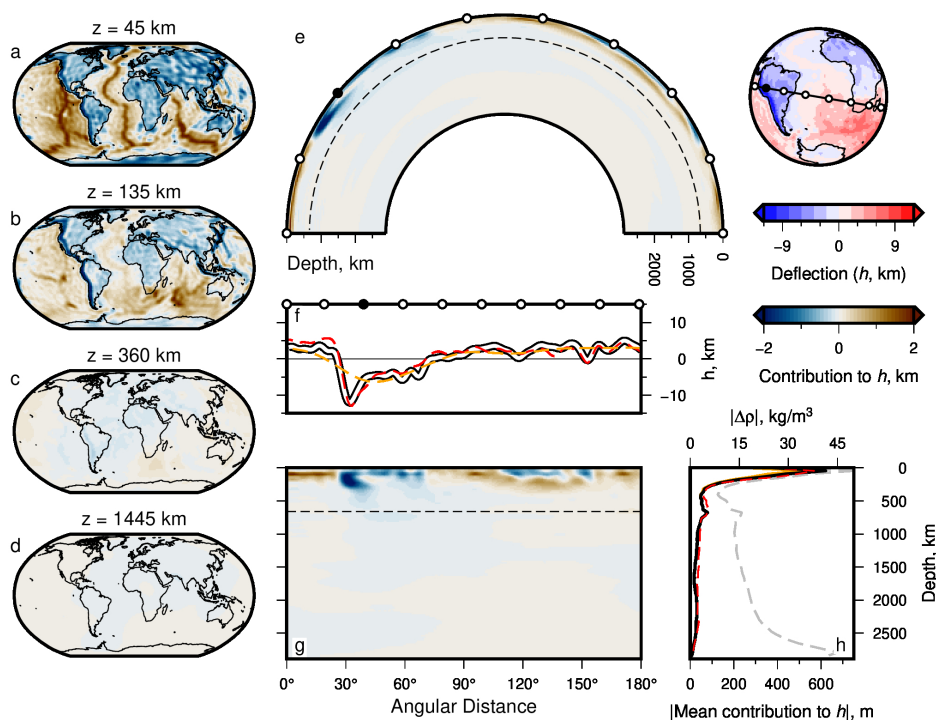


**Figure 9. Effective density; contributions from density anomalies to surface deflection.** (a–d) Maps of net contribution to present-day water-loaded surface deflection calculated using propagator matrix approach (Model 12; see body text for details). Depth slices at 45, 135, 360 and 1445 km depth incorporating all spherical harmonic degrees  $l$  and orders  $m$ , up to  $l = 50$ . (e) Great-circle slice ( $180^\circ$ ) showing contributions to surface deflection; globe to right shows transect location and calculated surface deflection (Model 12). White circles =  $20^\circ$  intervals; note filled black circle for orientation; dashed line = 660 km depth contour. (f) White-black curve = total surface deflection along transect shown atop globe in panel (e); abscissa aligned with panel g; orange dashed line = same but for maximum  $l = 10$  (see Supporting Information Figure S18); red dashed curve = surface deflection from Model 2. (g) Cartesian version of panel (e); ordinate aligned with panel (h). (h) Grey dashed curve = mean absolute value of density anomalies in Model 12—see top axis for values. Black curve = global mean amplitude (modulus) of contribution from density structure in Model 12 to total surface deflection  $h$ , across all  $l$  and  $m$ ; orange line = same but for maximum  $l = 10$ ; red dashed line = results for Model 2 (see Section 6.3). See Figures S15–S19 for extended results, demonstrating sensitivity of surface deflections to maximum spherical harmonic degree.